ACS Catalysis

pubs.acs.org/acscatalysis
Research Article

Elucidating Mn Promoter Structures and Stability on Co Nanoparticles through a Machine Learning Potential-Powered Genetic Algorithm

Enrico Sireci, Julie-Ann Hoffman, Dmitry I. Sharapa, Thobani G. Gambu, Eric van Steen, and Felix Studt*

Cite This: https://doi.org/10.1021/acscatal.6c04886
Read Online

ABSTRACT: Mn promotion has emerged as a prominent route to deliver the next-generation Co Fischer–Tropsch (FT) catalysts, urgently needed to scale up the production of aviation fuels. Nonetheless, to date, the underlying promotional mechanism has not been fully understood. While theoretical calculations have been previously carried out to address this task, the choice of the models has so far been limited, leaving possibly important factors unexplored. In this work, we have employed a genetic algorithm (GA) powered by machine learning potential (MLP) to optimize Mn structures on realistic models of 6–8 nm fcc and hcp Co nanoparticles (NPs) obtained via our recently published DFT–Monte Carlo (MC) approach. The resulting phase diagrams indicate that Mn structures are hydroxylated during FT, while their stoichiometry after activation is MnO–$MnO_{1.5}$. Mn was found to strongly bind to the Co NPs, although increasing loading considerably weakened the metal–promoter interactions. The structural characterization of the low-energy candidates produced during the GA runs revealed that Mn forms monolayer-like, mostly amorphous patches on the Co surface, which largely influences the promoter structures. Furthermore, we observed that Mn preferentially binds to the Co low-coordinate sites (LCS), which become almost fully covered already at the lowest investigated promoter loading. Last, we employed a magnetic moment–oxidation state correlation to predict the charge of Mn in our models, which was found to always be roughly 2+ regardless of the NP model, Mn phase, and loading. This was ascribed to a charge compensation mechanism involving the Co surface, which keeps Mn in the particularly favorable 2+ electronic configuration despite the actual promoter phase stoichiometry.

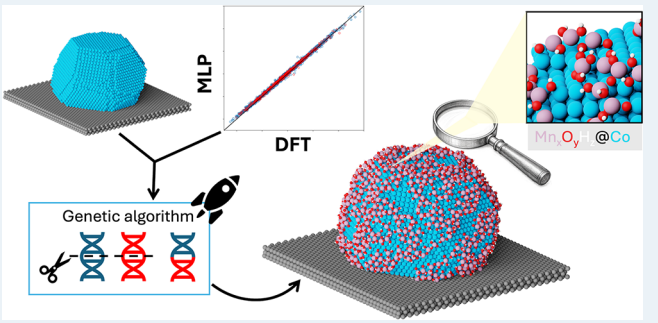

KEYWORDS: *cobalt nanoparticles, Mn promotion, Fischer–Tropsch, DFT, MLP, genetic algorithm*

1. INTRODUCTION

The Fischer–Tropsch (FT) process is experiencing renewed interest and growth owing to the urgency of abating global CO_2 emissions, especially in the aviation sector. The FT synthesis, in fact, can be integrated in a sustainable process using syngas obtained from renewable sources (e.g., from biomass gasification or carbon capture coupled with water electrolysis) to produce green fuels.[1−6]

Fe-[7,8] and Co-based[9−13] catalysts are conventionally employed in industrial FT reactors, with the latter being particularly suitable for sustainable aviation fuel (SAF) production due to their high activity and high C_{5+} selectivity at mild temperatures (500 K). A prominent route to optimize Co catalysts is the addition of moderate amounts of Mn during catalyst preparation, which has been shown to boost catalyst activity and especially C_{5+} selectivity.[14−27] Further reported effects of Mn addition are lower reducibility of the catalyst, often ascribed to Mn incorporation in the Co oxide precursor, and a moderate decrease in the Co particle size.[14,24,28] Mn promotion might additionally play a role in the competition between the fcc and hcp Co crystal phases.[29] Despite this, the underlying promotional mechanism remains unclear. Albeit a tangible part of the Mn loading is deposited on the oxidic support (often SiO_2, TiO_2, or Al_2O_3), studies employing elemental mapping of Mn-promoted Co catalysts report intimate contact between the two elements.[14,15,18,19,21,26,30] Furthermore, reduced H_2 uptake with increasing Mn loading indicates that the promoter partially covers the Co surface,[17,21,22] a conclusion supported by the fact that the addition of too much Mn becomes detrimental for activity, presumably because it starts to encapsulate the Co particles. The Mn species likely function synergistically with

Received: June 24, 2026
Revised: August 27, 2026
Accepted: August 27, 2026

the Co surface on which they are deposited and alter the reaction energetics, with experimental studies reporting enhanced CO adsorption and dissociation upon Mn addition.[15,17,31]

Previous computational studies have attempted to clarify the role of Mn by calculating relevant reaction steps of the FT reaction network such as CO dissociation and O removal on Mn-promoted Co surfaces.[14,16,17,22,32,33] While this provides significant insights, limitations inherent to the adopted models greatly reduce their transferability to real catalytic systems. In the following, we list the most critical. First, several models of Mn on Co surfaces have been previously proposed ranging from metallic Mn alloying with Co[22,34] to atomically dispersed oxidic Mn,[14] cluster,[16,17] and periodic structures[32,33] decorating the Co surface. Nonetheless, the choice of these models has often been rather arbitrary despite determining to a large extent the outcomes of the simulations, with different studies drawing different qualitative conclusions. The works by Kimpel et al.[17] and Chen et al.[32] stand out in that they attempted to mitigate user bias by employing global optimization (GO) methods to define their models, even though their exploration of the potential energy surface (PES) has been limited in terms of stoichiometries (i.e., Mn:O:H ratios) as well as Mn loadings. Furthermore, most of the previous studies have considered structures with a Mn:O ratio of 1, in light of the widely reported experimental Mn oxidation state of 2+.[15,17,35] On the other hand, Tucker et al.[14] have revealed through DFT-based thermodynamic analysis that a O–Mn–O cluster would be the most favorable configuration under FT conditions, suggesting that the oxygens could draw charge from the Co surface so that Mn retains a 2+ oxidation state. Moreover, by using periodic models, the previous studies could not unambiguously link the number of simulated Mn atoms to the experimental loading, hence overlooking its effect on promoter speciation. A further critical point is that only Mn structures on Co(111) or (0001) terraces have previously been considered. Nonetheless, experimental and theoretical studies have shown that CO dissociation on unpromoted Co catalysts occurs on the undercoordinated sites of the metal nanoparticles (NPs) such as steps and kinks.[36−43] Given the reported increase of the rate of CO dissociation upon promotion, this evidence suggests that Mn might interact with the Co low-coordinated sites (LCS).

In this work, we employ DFT calculations and a machine learning potential (MLP)-powered genetic algorithm (GA) to produce models of Mn structures on Co NPs. Our starting point is realistic models of fcc and hcp Co NPs obtained via our recently published DFT–Monte Carlo workflow,[44,45] which are used as surfaces in the GA. We considered 6 and 8 nm fcc–Co and 8 nm hcp–Co particles, which were cut along their symmetry planes to reduce the computational cost. On these, we investigated five different Mn:O:H stoichiometries as well as Mn:Co molar ratios ranging from 0.01 to 0.05, which are within the usual experimental Mn loading range. We employed a DFT-based thermodynamic analysis to build phase diagrams of Mn both at FT and reduction conditions and further investigated the Mn structures and preferential location on the Co particles. By employing a DFT-derived correlation of Mn atomic magnetic moments vs formal charge,[46] we additionally predict the correspondence between experimental Mn oxidation state and actual stoichiometry. By employing a GO method, we considerably alleviated user bias in the exploration of the PES, while the inclusion of NP surfaces and the comprehensive investigation of Mn stoichiometries and loadings ensures that the gap between computational models and technical catalysts is greatly reduced in comparison to the state of the art. The comprehensive modeling workflow elaborated here significantly advances the current understanding of Mn structures on Co catalysts and offers new insights into the promotional effects of Mn.

2. COMPUTATIONAL METHODS

In Figure 1, we show a schematic representation of the computational workflow carried out in this study. The large size of the investigated systems dictates the use of a cheap method as internal calculator in the GA runs. We have chosen for this task the universal MLP CHGNet,[47] which offers the advantage of predicting, in addition to energy and forces, also the magnetic moments of the atoms in the calculated structures. This feature is particularly relevant for our case study since, as it will be shown in Section 3.3, we can use the Mn magnetic moment to derive its formal oxidation state. We note that MLPs have been previously employed as internal calculators in GA optimizations.[48−50] The original CHGNet potential was fine-tuned on a dataset covering a configurational space relevant for our application. The strategy carried out to create the dataset (green box in Figure 1) is described in Section 2.3 and relies on the extraction of a diverse set of configurations from GA runs employing the original CHGNet potential on periodic fcc–Co surfaces. These were labeled via DFT single-point (SP) calculations with the methods presented in Section 2.2. Upon fine-tuning the MLP (red box in Figure 1) and validating its accuracy, we finally employed it as a calculator in the GA production runs (blue box of Figure 1), described in Section 2.1 which yielded the relevant low-energy structures discussed in Section 3.

2.1. GA Calculations

To the best of our knowledge, here we report for the first time a GA approach to optimize chemical structures using portions of metal NP shells as slab models. The starting point to build these was the outcomes of our recently published DFT-Monte Carlo simulations, which distribute Co atoms in a fixed fcc or hcp grid to predict low-energy structures of metal NPs. We direct the reader to our previous works for further details about the methodology.[44,45] Here, we considered 6 and 8 nm fcc–Co and 8 nm hcp–Co NPs. These particle sizes are particularly relevant with respect to industrial Co FT catalysts, for which the typical target for the center of the particle size distribution lies around 8 nm.[51] This is because particles smaller than 3.5–4 nm are prone to deactivation[52−54] and do not meet the activity requirements, while particles larger than 8 nm result in lower Co dispersion against no benefit in terms of catalytic performance.[40,55−57] Even though simulating also 10 nm NPs would have enlarged the scope of our work, the higher number of atoms makes them particularly cumbersome to model. For each particle model, 40 parallel Monte Carlo runs are carried out, each yielding one lowest-energy structure. From these, we selected the one with the energy closest to the average over the 40 structures as it was assumed to be the most representative. In order to reduce the computational cost, we cut the NPs along their symmetry planes to produce models that are roughly 1/4 and 1/8 of the original 6 and 8 nm particles, respectively. Additionally, we carved out a portion of the inner Co atoms while making sure that the resulting NP shell is at all points at least four Co layers thick. The resulting NP slabs contain roughly 2000 Co atoms. To avoid spurious interactions owing to Mn clusters migrating over the artificial edges of the models, these were covered with He atoms that provided steric hindrance. All the He atoms as well as the Co atoms at the cut locations and in the two innermost layers of the employed NP shells were frozen during optimization, while the two top layers of Co atoms were allowed to relax. Snapshots of the employed slab models are given in Figure 2. The energies of the different MnO_xH_y@Co phases reported throughout this work are predicted from the global minima (GM) structures identified in each run upon removal of the He atoms. Since the interactions between the Mn units close to the edges and the He atoms could yield

https://doi.org/10.1021/acscatal.6c04886
ACS Catal. XXXX, XXX, XXX−XXX

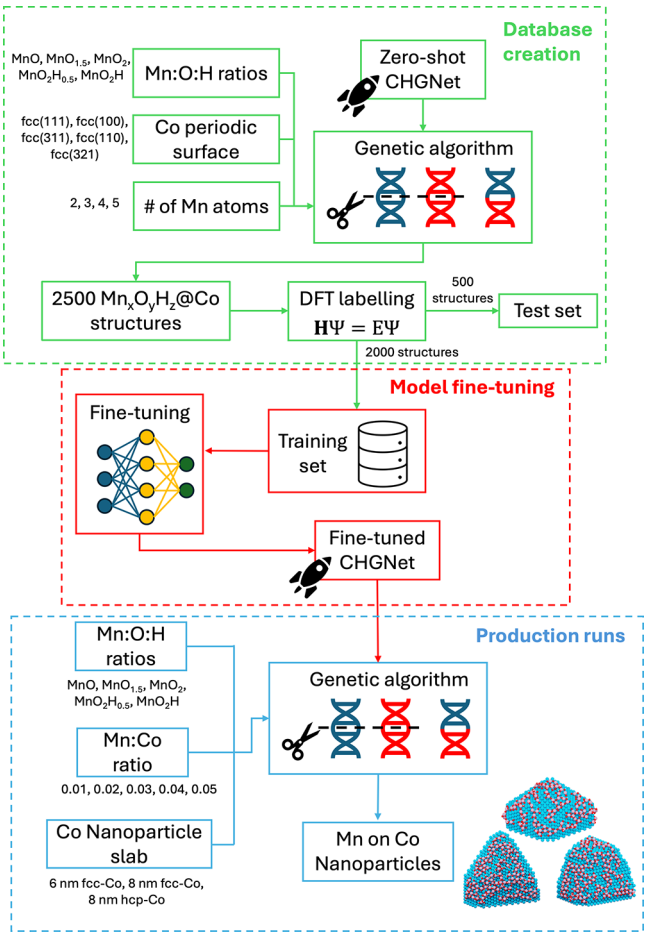

Figure 1. Schematic illustration of the workflow employed in this work.

small energy contributions (up to 0.1 eV), we removed them to slightly increase the accuracy of the predictions.

We employed a modified pool-based version of the atomic simulation environment (ASE) GA[58,59] with a population of 30 candidates. The initial population was generated by performing a simple iterative algorithm that works as follows: a $Mn_xO_yH_z$ formula unit is placed at a random position in the unit cell; if the distance between this position and the closest Co atom is ≤4 Å and the atoms of the unit are not in close contact with any other atom (including those from previously placed units and Co atoms), the $Mn_xO_yH_z$ cluster addition is accepted and the algorithm proceeds to place a new unit; if the above criteria are not met, a new random position is chosen until a valid position is identified. The algorithm proceeds until the desired number of Mn atoms has been placed in the unit cell. The pairing procedure was carried out via a cut-and-splice operation, where parents were selected based on their fitness, which depends on their energetic stability and how frequently they have already been selected for offspring generation. In our implementation, the cutting plane used in the pairing procedure could break Mn–O, Mn–OH, or O–H bonds, causing the offspring to sometimes display isolated O, H, or OH. To alleviate this, after the pairing procedure, O that are further away than 2.5 Å from any Mn atom are randomly placed next to a Mn with the fewest O neighbors; similarly, H atoms that are not within 1.2 Å from the closest O atom are placed next to a randomly chosen dehydroxylated O atom. A schematic illustration of the procedure is given in Figure S1. This avoids generating structures where O and H atoms bind to Co independently from the Mn clusters, which are not the subject of this study. Furthermore, this allows for rearrangement of O and H during the run, which increases diversity in the population pool. Before relaxation, a mutation is performed on

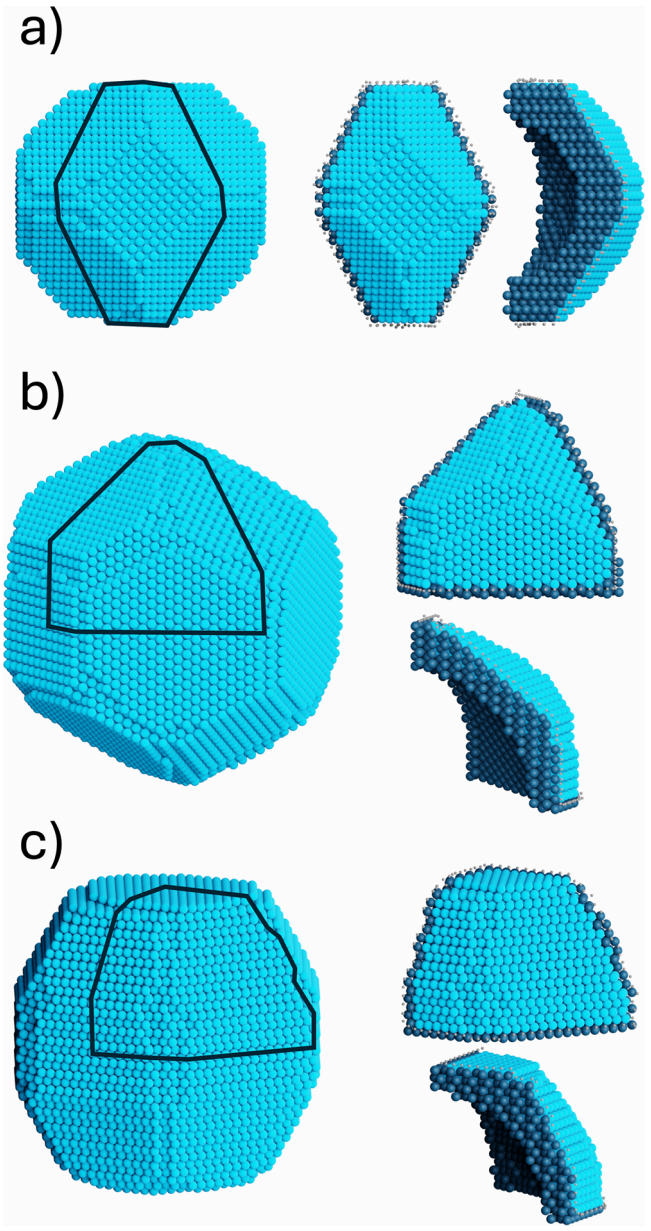

Figure 2. Nanoparticles (left) and frontal and side views (right) of corresponding slab models employed in the GA runs for (a) 6 nm fcc–Co, (b) 8 nm fcc–Co, and (c) 8 nm hcp–Co. Frozen Co and He atoms are depicted in dark blue and gray, respectively.

the offspring with a probability of 0.35. We employed the classical rattle mutation and a custom mutation that moves $Mn_xO_yH_z$ units to unoccupied low-coordinated Co atoms in the slab, performed in a probability ratio of 1:4. The custom mutation identifies the terminal O (namely, those that bind to only one Mn atom) in the structure and moves the corresponding Mn–O pairs with a 50% and a 100% probability for Mn loadings ≤0.03 and >0.03, respectively, to the low-coordinated Co atoms. If O or OH groups remain isolated as a result of the displacement of the Mn–O pairs, they are placed next to the Mn atoms that had been previously moved. We note that this custom mutation does not introduce a systematic search bias toward specific structural motifs, since the mutant candidates are still subject to fitness evaluation that determines whether they are included in the population pool. Hence, they will be allowed to propagate their genetic makeup only if they are particularly stable and unique. Upon relaxation, the offspring is added to the population if it is significantly different from all the

https://doi.org/10.1021/acscatal.6c04886
ACS Catal. XXXX, XXX, XXX–XXX

current candidates and more stable than the least stable among them, which is consequently replaced. Following the work of Vilhelmsen and Hammer,[58,59] a sorted list D_i of all interatomic distances is calculated for each i candidate. Two candidates are considered identical if

$$\frac{\Sigma_k |D_i(k)-D_j(k)|}{\frac{1}{2}(\Sigma_k D_i(k)-D_j(k))} < \delta_{rel} \quad (1)$$

$$\max_k(|D_i(k) - D_j(k)|) < d_{max} \quad (2)$$

and

$$|E_i-E_j| < 0.1 \text{ eV} \quad (3)$$

where δ_{rel} is the relative accumulated difference, here set to 0.25 Å, while δ_{max} is the maximum difference between two distances, here set to 3.0 Å. E_i and E_j are the potential energies of candidate i and j, respectively. We note that the cutoff values of the parameters assessing similarity across different structures typically used for the optimization of small clusters (i.e., ∼0.02 eV, 0.03, and 0.7 Å for dE, δ_{rel}, and δ_{max}, respectively)[59−61] are significantly smaller than those employed here, which were scaled up according to the larger size of the investigated structures. Using standard parameters, in fact, would cause the algorithm to classify as distinct candidates with structural and energetic differences that are negligible for the purpose of this study, which would in turn favor stagnation around local minima basins. Candidates were relaxed until the maximum force in the system was below 0.075 eV/Å. A pre-relaxation with the original MLP of 20–40 ionic steps depending on Mn loading was performed on all candidates, which was necessary to get rid of unphysical geometries often present right after the pairing and which sometimes caused the fine-tuned potential, which is less robust, to fail. In the rare event that the fine-tuned potential still failed after the pre-relaxation, the structure was discarded and a new offspring was generated. We additionally applied an energy-based screening of the candidates, which made the algorithm discard those that, after a few dozen ionic steps, were still energetically significantly less stable than the current global minimum (GM). Convergence was achieved when in the last 600 candidates no structure more stable than 5 meV/Mn than the previously identified GM was proposed. Plots showing the progression (energy vs candidate #) of all the GA runs are given in the Supporting Information accompanying this article, along with relevant scripts and with trajectory files containing the relaxed candidates of all the GA runs. We investigated 5 Mn stoichiometries with formula units MnO, $MnO_{1.5}$, MnO_2, $MnO_2H_{0.5}$, and MnO_2H. For each stoichiometry, we considered five different Mn loadings with Mn:Co molar ratios of 0.01, 0.02, 0.03, 0.04, and 0.05, which correspond to 25, 50, 75, 100, and 125 Mn atoms for the 6 nm fcc–Co slab and 30, 60, 90, 120, and 150 Mn atoms for the 8 nm fcc and hcp–Co slabs. These numbers were obtained by considering the total number of Co atoms (10,152 and 24,064 for the 6 and 8 nm NPs, respectively) in the whole, uncarved particles and calculating the corresponding number of Mn atoms, which were further divided by 4 and 8 for the 6 and 8 nm slab models, respectively. Last, we note that in this study we only focused on Mn (hydro)oxide species decorating Co^0 NPs and neglected possible Mn–Co alloys as well as mixed oxide NPs. This choice is motivated by numerous reports indicating that, in activated Mn–promoted Co FT catalysts, Mn and Co are predominantly found in the 2+ and metallic states, respectively.[15,17,32,35] We note, however, that the fresh catalyst typically contains Mn–Co mixed oxide NPs, some of which (presumably the smaller ones) likely persist after reduction. These, however, are not expected to be active in the FT synthesis, as the presence of Co^0 where CO can adsorb strongly is required for catalytic activity, hence motivating our focus on Mn (hydro)oxide species adsorbed on Co^0 NPs.

2.2. DFT Calculations

Spin-polarized DFT calculations were performed within the VASP code version 6.2,[62,63] employing the GGA functional BEEF-vdW[64] and using the projector-augmented wave (PAW) method with standard PAW potentials.[65] Gaussian smearing with a width of 0.1 eV and an energy cutoff of 400 eV were used in all calculations. The sampling of the Brillouin zone was carried out using a Monkhorst–Pack grid with a k-points density of ∼36 k-points·$Å^{-1}$. For the model fine tuning (explained below), we have carried out DFT single-point calculations of $Mn_xO_yH_z$ structures adsorbed on

- a p(4 × 4) Co(111) slab using a 4 × 4 × 1 k-point grid,
- a p(4 × 4) Co(100) slab using a 4 × 4 × 1 k-point grid,
- a p(2 × 4) Co(110) slab using a 5 × 4 × 1 k-point grid,
- a p(2 × 2) Co(311) slab using a 3 × 4 × 1 k-point grid,
- and a p(2 × 2) Co(321) slab using a 3 × 2 × 1 k-point grid.

The unit cell z dimensions were varied to ensure that the Co slabs were separated by 20 Å of vacuum from their periodic images. Convergence of the SCF cycle was set at an energy difference of 10^{-6} eV, while ionic convergence—relative to the geometry optimizations of the investigated $Mn_xO_yH_z$ structures adsorbed on α-SiO_2(001), γ-Al_2O_3(110), and anatase TiO_2(101)—was achieved when atomic forces were below 0.01 eV/Å. An on-site Coulomb repulsion correction term for the 3d orbitals of the Mn atoms was applied through the Hubbard correction in the rotationally invariant approach introduced by Dudarev et al. with U_{eff} = 2.5 eV.[66] This value was obtained upon calibration of the theoretical vs experimental standard enthalpies of reaction (ΔH^0_{rxn}) at T = 298 K of bulk MnO oxidation to its higher oxides, as shown in our previous work.[46] The atomic magnetic moments of Co and Mn atoms were always initialized with values of 2.5 and 5.0 μ_B, respectively. The former consistently converged on values in the 1.6–1.7 μ_B range, while the latter converged on the preferred high–spin configuration relative to the specific oxidation state of Mn, which was predominantly 2+ and resulted in magnetic moments in the 4.2–4.5 μ_B range.[46] The gas-phase molecules considered in this study, i.e., H_2 and H_2O, were optimized in cubic boxes with a side length of 20 Å employing only one k-point. Vibrational analysis to estimate thermal corrections for the gas-phase molecules as well as for adsorbed O and OH groups were carried out with the finite-differences method with a displacement of 0.02 Å.

2.3. Dataset Creation and MLP Fine Tuning

We fine-tuned the original CHGNet on a dataset of Mn clusters on Co surfaces, whose energies, forces, and magnetic moments were evaluated at the GGA-DFT level of theory via SP calculations with the methods reported in Section 2.2. The dataset was built by performing GA runs, employing the original CHGNet potential as internal calculator, optimizing $Mn_xO_yH_z$ structures on fcc–Co periodic surfaces, and by extracting from each run 25 structurally diverse configurations, of which 5 were stored as a test set. We performed 100 GA runs, from which we extracted a total of 2000 structures for the training set and 500 for the test set, including

- five $Mn_xO_yH_z$ stoichiometries, with formula units: MnO, $MnO_{1.5}$, MnO_2, $MnO_2H_{0.5}$, and MnO_2H;
- four different Mn loadings, ranging from 2 to 5 Mn atoms;
- five different periodic fcc–Co surfaces, namely, (111), (100), (110), (311), and (321).

In the GA runs to create the database structures, we set dE, δ_{rel}, and δ_{max} to 0.1 eV, 0.025, and 0.3 Å, respectively, and have employed a mutation probability of 0.35 including the rattle,[67] mirror,[59] and permutation mutations,[68,69] all in the same proportions. We extracted the 25 structures from each GA run trajectory consisting of all relaxed candidates using the InteratomicDistanceComparator class from the standard comparators module of the ase.ga package, where the selected structures were characterized by an energy spacing–starting from the

https://doi.org/10.1021/acscatal.6c04886
ACS Catal. XXXX, XXX, XXX−XXX

most stable candidate—of 0.05, 0.075, 0.1, and 0.125 eV in case the optimization cluster included two, three, four, and five Mn atoms, respectively. These criteria were found to yield an ensemble of significantly diverse database structures. Snapshots of five sample database structures obtained from the GA runs are shown in Figure S2. In addition, we included geometry optimization trajectories of previously calculated Mn clusters on Co surfaces, clean Co slabs and fcc–Co, and Mn oxide bulk structures. The final size of the employed training set was ∼2500 structures. Eighteen additional GA runs including three stoichiometries (MnO, MnO_2, and MnO_2H), two Mn loadings (two and four atoms), and three hcp–Co surfaces (10–10, 10–11, and 10–12) were carried out to extract 360 more structures, which were only included in the test set. The training data set is provided separately both as json and ase db files. The dataset, excluding the 500 $Mn_xO_yH_z$@fcc–Co and 360 $Mn_xO_yH_z$@hcp–Co test structures, was randomly split into training (90%), validation (5%), and test (5%) sets with a batch size of 8. Transfer learning was employed by freezing the embedding layers and the majority of the graph convolution layers, while optimizing the remaining layers. Training was performed for 2400 epochs using the Adam optimizer with a learning rate of 5E-3, a cosine learning rate scheduler, and a mean squared error loss function applied to energies, forces, and magnetic moments. The fine-tuned potential obtained after the training procedure was characterized by mean absolute errors (MAEs) of 1 meV/atom, 20 meV/Å, and 8 $m\mu_B$/atom for energies, forces, and magnetic moments, respectively, which are in the accuracy range of typical application-specific MLPs.[70−77] Additionally, the fine-tuned potential faithfully reproduces the Co–Co bond lengths in bulk fcc–Co, with a difference of only 0.002 Å (i.e., ∼0.1%) with respect to DFT.

We were furthermore interested in assessing the MLP accuracy in terms of formation energies of Mn clusters according to the following equations:

$$x\mathrm{MnO}_{(\mathrm{bulk})} + y\mathrm{H_2O}_{(g)} + \mathrm{Co}_{\mathrm{slab}} \rightarrow \mathrm{Mn}_x\mathrm{O}_{x+y}\mathrm{H}_z@\mathrm{Co}_{\mathrm{slab}} + (y - {}^1/_2 z)\mathrm{H_2} \quad (4)$$

$$\Delta E^{\mathrm{f}} = (E_{\mathrm{Mn}_x\mathrm{O}_{x+y}\mathrm{H}_z@\mathrm{Co}_{\mathrm{slab}}} + (y - {}^1/_2 z) E_{\mathrm{H_2}} - E_{\mathrm{Co}_{\mathrm{slab}}} - yE_{\mathrm{H_2O}} - xE_{\mathrm{MnO}_{(\mathrm{bulk})}})/x \quad (5)$$

As evident from the comparison between the parity plots in Figure 3a,b, the fine-tuning procedure led to a dramatic improvement of MLP performance as the MAE of ΔE^{f} decreases from 271 to 25 meV/Mn atom between the zero-shot and the fine-tuned CHGNet potential. It is worth noting that the test set reported in Figure 3 consists of the previously stored 500 $Mn_xO_yH_z$@fcc–Co, which were not included in the training set. Furthermore, we observe from Figure 3b that the accuracy of the fine-tuned potential is converged with training set size, as it performs equally well on the training and test sets. Analogous parity plots relative to the unnormalized ΔE^{f} (i.e., the formation energy as calculated per eq 5 multiplied by the number of Mn atoms in the structure) are reported in Figure S3 with MAEs of 83 and 84 meV for the training and test sets, respectively. We additionally report in Figure S4 parity plots relative to force predictions—which are equally important to assess the quality of the MLP—for which we found MAEs of 15 and 24 meV/Å for the training and test sets, respectively. We point out that while the fine-tuning procedure can be rather laborious (it involves dozens of GA runs to create the structure database in addition to thousands of DFT single-point calculations), the effort is well-justified by the fact that it ultimately enables near DFT accuracy accompanied by a massive computational speedup.

In Figure S5, we additionally report the parity plot between $Mn_xO_yH_z$@hcp–Co cluster formation energies calculated with DFT and the tuned CHGNet potential. The MAE relative to these

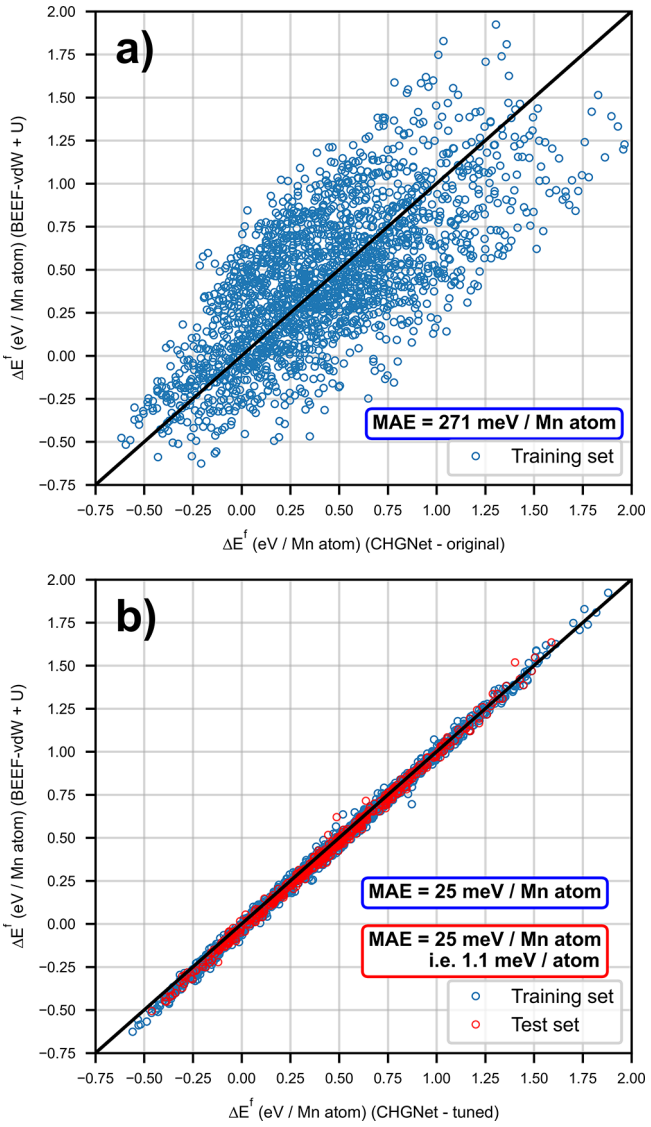

Figure 3. Parity plots of $Mn_xO_yH_z$@fcc–Co cluster formation energies as defined in eq 5 calculated with DFT and (a) the zero-shot and (b) the fine-tuned CHGNet MLP. The data points in (a) were all shifted by a constant energy that minimized the MAE, so that systematic errors coming from inaccurate zero-shot CHGNet calculation of the reference structures are not considered.

structures (74 meV/Mn atom) is significantly larger than for those on fcc–Co, which can be readily explained by the fact that hcp–Co structures were not included in the training dataset causing the fine-tuned potential to not capture the adsorption of the $Mn_xO_yH_z$ on hcp motifs as accurately as on fcc ones. Interestingly, however, the error is still smaller by roughly a factor 4 in comparison to the zero-shot potential, which indicates that the fine-tuning considerably improves the accuracy even when calculating previously unknown surfaces and suggests that the ML architecture possess a certain extrapolation capability. Moreover, it is clear from Figure S5 that most of the error comes from a systematic overstabilization of the structures calculated with the MLP as compared with DFT, indicating that the predictions of the relative stabilities are still very accurate. The systematic overstabilization of $MnxO_yH_z$–hcp–Co structures may arise from either an inaccurate description of bare hcp–Co or an overestimation of the $MnxO_yH_z$–hcp–Co interaction. Since the bare hcp–Co slab is present in both the reference and supported systems, partial error

https://doi.org/10.1021/acscatal.6c04886
ACS Catal. XXXX, XXX, XXX−XXX

cancellation would be expected in the former case, suggesting that the interaction with the hcp–Co surface is likely responsible, at least in part. Further improvements of the model could likely be obtained by the inclusion of hcp–Co structures.

3. RESULTS AND DISCUSSION

3.1. Stability of Mn on Co NPs

In Figure 4, we present the phase diagrams of $Mn_xO_yH_z$@Co in the FT gas phase (feed of 20 bar, H_2:CO = 2:1) and snapshots of the most stable phase at typical FT conditions of T = 500 K, X_{CO} = 75% on the three different NP models investigated for Mn:Co = 0.01, 0.03, and 0.05. In Figure S6, we show all the phase diagrams including those for Mn:Co = 0.02 and 0.04. The phase diagrams were built considering the Gibbs free energies of formation (ΔG^f) of the global minima (without He atoms) identified in each run that were calculated as follows:

$$\Delta G^f_{GM}(Mn_xO_yH_z) = G_{GM} + \left(y - {}^1/_2 z\right)\mu_{H_2} - y\mu_{H_2O} - xE_{MnO_{(bulk)}} - E_{Co_{slab}} \quad (6)$$

where $\Delta G^f_{GM}(Mn_xO_yH_z)$ is the Gibbs free energy of formation of the GM structure with a given stoichiometry, G_{GM} is the Gibbs free energy of the GM (potential energy + thermal corrections), μ_{H_2} and μ_{H_2O} are the chemical potential of gas-phase H_2 and H_2O, respectively, $E_{MnO_{(bulk)}}$ is the potential energy of bulk MnO, and $E_{Co_{slab}}$ is the potential energy of the Co NP slab.

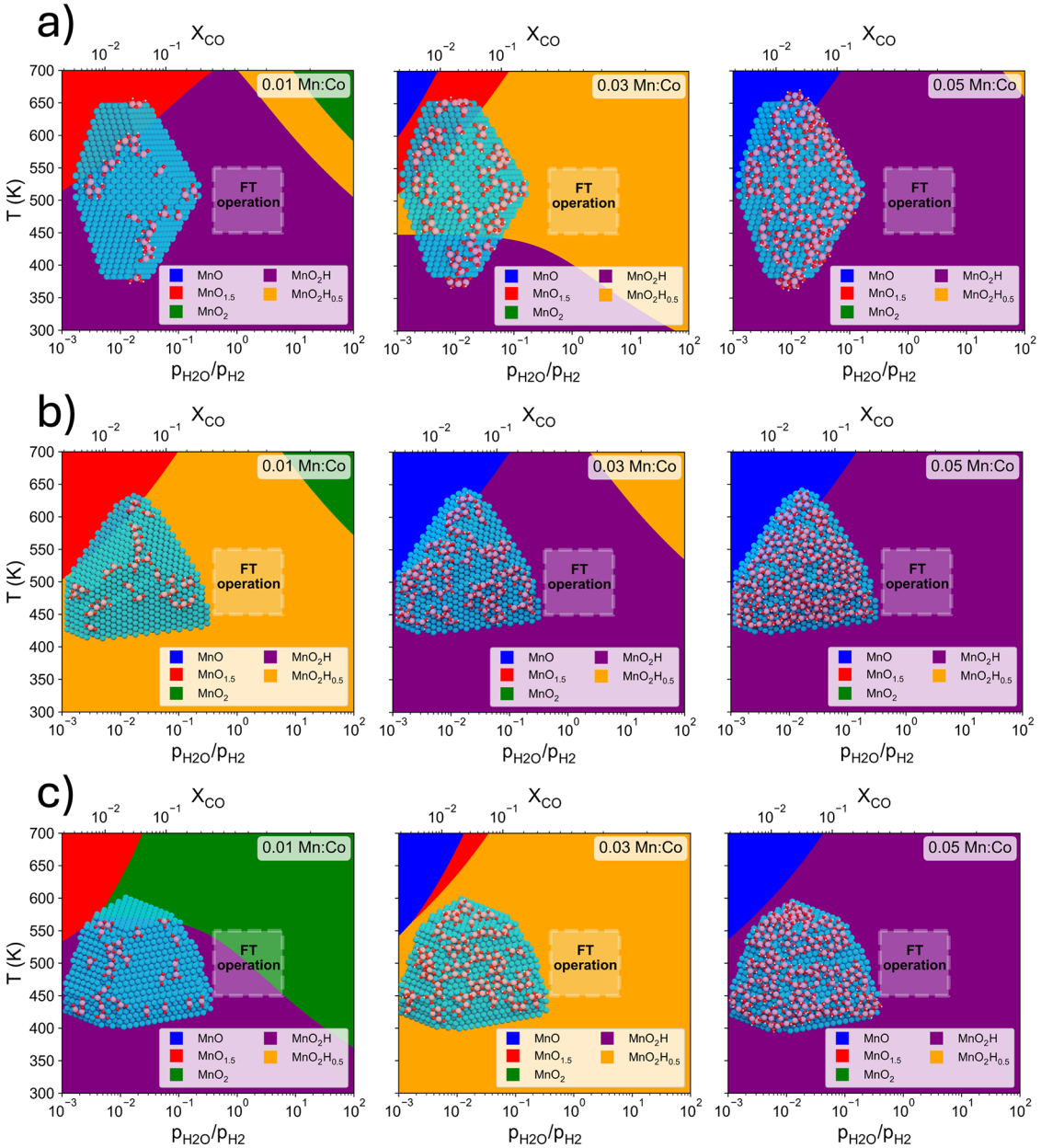

Figure 4. Phase diagrams of Mn structures with loadings ranging from 0.01 to 0.05 Mn:Co on (a) 6 nm fcc–Co NP slab, (b) 8 nm fcc–Co NP slab, and (c) 8 nm hcp–Co slab. Snapshots of the most stable phases under FT conditions are shown as insets in the respective phase diagrams.

https://doi.org/10.1021/acscatal.6c04886
ACS Catal. XXXX, XXX, XXX–XXX

The $ZPE + \Delta H^{0\rightarrow T} - T\Delta S$ contributions were included for the gas-phase molecules as well as for the calculated GM structures. For the latter, we accounted for the thermal corrections relative to adsorbed O and OH groups, which were calculated within the harmonic approximation and as a function of temperature from two hypothetical mononuclear MnO_2 and MnO_2H clusters adsorbed on fcc–Co(111), whose vibrations were calculated with DFT. The resulting curves relative to the $ZPE + \Delta H^{0\rightarrow T} - T\Delta S$ contributions per adsorbed O and OH group as a function of temperature are presented in Figure S7. Within this approach, we hence assume that the free energy corrections relative to adsorbed O and OH groups do not change across the considered structures. To verify the validity of this assumption, we compared the total free energy corrections as calculated with our approach and with explicit DFT vibrational analysis at 500 K for the two pyramidal Mn clusters adsorbed on the α-SiO_2 and TiO_2 supports shown in Figure S13, each containing 12 OH groups. We obtained overall differences of 102 and 73 meV (or 8.5 and 6.1 meV/OH group) for the α-SiO_2- and TiO_2-supported structures, respectively, suggesting that our approach to free energy corrections does not introduce significant errors.

For each Co slab, five different Mn:Co ratios ranging from 0.01 to 0.05 were investigated. Since most studies report optimal Mn:Co ratios between 0.05 and 0.1,[14,15,19] and considering that a relevant fraction of Mn is often observed on the support, we argue that the investigated loading range is representative of commonly synthesized Mn-promoted Co catalysts. In Figure S8, we present analogous phase diagrams and snapshots of Mn@Co under reduction conditions (feed of 1 bar, pure H_2), while in Figures S9–S11, we show the $\Delta G^{f}_{GM}(Mn_xO_yH_z)$ at different loadings with increasing p_{H2O}/p_{H2} ratios and fixed $T = 500$ K as well as at fixed $p_{H2O}/p_{H2} = 2.1$ and increasing T on the three Co NP models.

Except for the lowest loading on the 8 nm hcp–Co slab, we find that the preferred Mn phases are always $MnO_2H_{0.5}$ or MnO_2H under reaction conditions, suggesting that the Mn structures possess hydroxyl functionalities that might have a role in the reaction network. In particular, it is likely that such functionalities can rearrange dynamically under reaction conditions and might be centers for hydrogen shuttling. This would enhance the hydrogenation reactions occurring during FT, such as CO hydrogenation to HCO or COH species—key-intermediates in the H-assisted CO dissociation mechanism—as well as hydrogenation of the growing hydrocarbon (HC) chains and O removal via water formation. Regarding the latter reaction step, theoretical calculations predicted that Mn would facilitate O removal,[14] which is in line with the experimentally observed excellent resistance against oxidation of the Mn-promoted Co catalysts under operation at high X_{CO},[78] where the large p_{H2O}/p_{H2} ratios drive the phase transition from Co^0 to CoO in the unpromoted catalysts.[52,79] Furthermore, the OH groups could themselves undergo hydrogenation and desorb as gas-phase water, creating O vacancies that can be filled by dissociating CO. Such a mechanism has been previously proposed and predicted to greatly enhance the CO dissociation rates on hcp–Co(0001) terraces.[17] It was alternatively postulated by Chen et al.,[32] who observed the presence of OH groups on the Mn-promoted catalyst via XPS, that H atoms are sequestrated by the Mn oxidic clusters and become unavailable for chain termination, thus favoring chain growth. The phase diagrams in Figure S8, however, show that the most stable Mn phases in the activated catalysts are always $MnO_{1.5}$ or MnO, indicating that the change in thermodynamic conditions between reduction and FT affects the state of Mn in the catalyst.

Figure 4 additionally reveals that Mn loading has a significant impact on the phase diagrams. Overall, we observe that increasing loading favors the formally more reduced Mn phases: the MnO_2 phase, which is observed only in the high T–high p_{H_2O}/p_{H_2} corners of the phase diagrams for the 0.01 Mn:Co ratio for the three slabs and the 0.02 Mn:Co ratio only for the 8 nm hcp–Co slab, disappears with increasing loading, and similarly, the $MnO_{1.5}$ phase is gradually taken over by MnO. $MnO_2H_{0.5}$ is also increasingly substituted by the MnO_2H phase for Mn:Co >0.02, even though the opposite trend emerges for Mn:Co ≤0.02 for the 6 nm fcc–Co and 8 nm hcp–Co slabs. These outliers are attributed to the fact that, as shown in Figures S5–S7, the two hydroxylated phases are generally very close in energy and thereby the difference can easily fall within the uncertainty of the calculations for the low loadings. The prevalence of the reduced phases with increasing Mn loading can be explained considering that, at higher coverages, the Mn centers are pushed closer together, forcing their agglomeration, which is likely less favorable for more oxidized structures due to electrostatic repulsion between the negatively charged ligands. Visual inspection of the GM snapshots in Figure 4 shows that for the Mn:Co ratios of 0.01, Mn is highly localized on the steps and edges of the NP slabs. At the higher loadings, however, also the terraces become densely populated. Overall, we observe a preference for formation of monolayer-like, mostly amorphous, Mn structures, whose structural patterns seem to largely be determined by the conformation of the Co NPs. For Mn:Co = 0.01–0.02, we prevalently observe either highly dispersed monoatomic or linear Mn structures, which mostly turn into 2D patches with increasing loadings. Additionally, we sampled 15 different Mn structural motifs on different Co surface conformations and transferred them to smaller periodic models, whose structures were subsequently relaxed with the fine-tuned CHGNet. Structural files in xyz format of the motifs are provided separately, while snapshots and their formation energies at FT conditions are given in Figure S12.

In Figure 5, we report the ΔG^{f} of the investigated Mn phases on the three considered NP models with changing Mn:Co ratio at FT conditions. These are also compared (dashed lines in Figure 5) with the ΔG^{f} of the most stable structures identified in this study formed by Mn on α-SiO_2(001), γ-Al_2O_3(110), and anatase TiO_2(101), which are representative of three common FT supports. These structures underwent geometry relaxation with DFT, which was also used to evaluate their stabilities. Details regarding all the calculated structures formed by Mn on the three supports are given in Table S1, while snapshots are presented in Figure S13. Structural files in xyz format are provided separately. Importantly, for all the phases but MnO, we witness a significant destabilization of Mn with increasing loading. In particular, the Mn structures are roughly 0.4, 0.3, and 0.2 eV/Mn atom less stable in the largest as compared to the lowest loadings for the MnO_2, $MnO_2H_{0.5}$, and both $MnO_{1.5}$ and MnO_2H phases, respectively. Hence, the destabilization of Mn with loading is more pronounced the more formally oxidized the Mn phase, which supports the idea that oxidation prevents agglomeration. The main reason for the observed

https://doi.org/10.1021/acscatal.6c04886
ACS Catal. XXXX, XXX, XXX–XXX

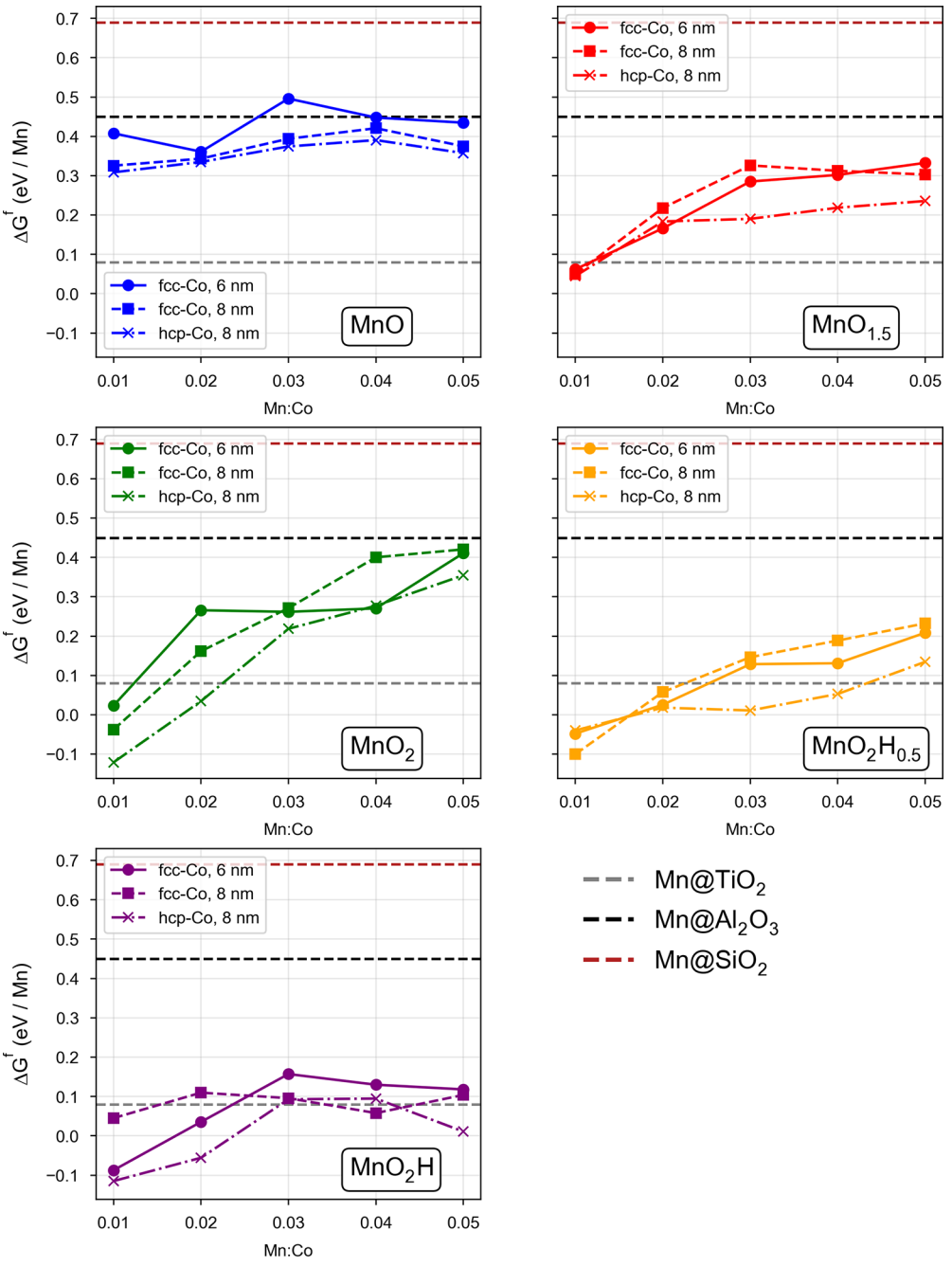

Figure 5. Formation Gibbs free energies (ΔG^f) normalized per number of Mn atoms calculated according to eq 6 at $T = 500$ K and $X_{CO} = 75\%$ of the investigated $Mn_xO_yH_z$ phases on the three Co NP slab models with increasing loadings.

destabilization is that the Mn oxidic clusters preferentially bind to the LCS on the Co NPs, which are found on the corners, edges, and steps. Since these sites, as will be shown in Section 3.2, are largely occupied already from the lowest loadings, further promoter addition results in coverage of the terraces, where it is less stable. This implies that a fraction of the Mn species covering the Co NPs is highly persistent, while another could more easily be washed away to the support, either during activation or, more likely, during FT, where Mn must compete for adsorption with strong binding CO molecules. We note that herein we neglect the effect of CO on the energetics of the Mn structures and only reference this to the H_2O/H_2 ratio. Highly reducing CO at elevated pressures might change the oxygen content of the $Mn_xO_yH_z$ clusters to some extent. Since we expect that this effect is similar across the different possible Mn phases, we argue that the energetic trends outlined here would still hold even when the structures are exposed to CO.

Comparing the stability of Mn on the three investigated supports, it is found that the promoter–support interactions are more favorable in the order anatase TiO_2 > γ-Al_2O_3 > α-SiO_2. Furthermore, while the $MnO_2H_{0.5}$–MnO_2H phases on Co NPs are always more stable than the Mn structures on γ-Al_2O_3 and α-SiO_2, for Mn:Co >0.02, they become either less

https://doi.org/10.1021/acscatal.6c04886
ACS Catal. XXXX, XXX, XXX–XXX

or roughly as stable as those on TiO_2. This means that more Mn deposits on the TiO_2 support compared to γ-Al_2O_3 and α-SiO_2. Additionally, the Co NP surfaces are unlikely to be extensively covered in these systems, as only a small portion of Mn forming highly stable structures will persist, while the promoter in excess eventually migrates to the support. Given that Mn tends to form mixed oxide particles with Co in the fresh catalyst, the portion that does not accommodate on the NPs after reduction might accumulate at the Co-support edges, which has been previously observed experimentally.[18] Furthermore, we note that recently Ivanez et al. have observed less extensive blocking of the Co surface by Mn when γ-Al_2O_3 was employed as support instead of SiO_2, presumably due to the stronger Mn–support interactions in the former, in line with the trend outlined here.[80]

Except for MnO in the Mn:Co = 0.01–0.02 range, in Figure 5 as well as in Figures S9–S11, we additionally observe that the ΔG^f of the different Mn phases are close to each other, with the energy differences at a given loading and NP model often not exceeding 0.1 eV/Mn atom. This suggests that the Mn structures can easily rearrange under FT conditions, which might be linked to their catalytic activity.

A comparison of the calculated ΔG^f across the investigated slab models indicates only a limited dependence of Mn stability on particle size and crystal phase, despite the investigated size range being rather limited. Although smaller nanoparticles contain a higher density of low-coordinated sites that stabilize the promoter structures, Figure S12 shows that Mn binds particularly strongly to stepped and kinked surface motifs (e.g., B5-A (311) and B6 (641)), whose abundance increases with particle size.[43] These competing effects may partially offset one another, which is consistent with the similar Mn stabilities predicted for the six and eight nm fcc–Co models. With regard to the fcc vs hcp competition, while the Mn structures are more stable on the 8 nm hcp–Co than on the 8 nm fcc–Co NP by an average (over the different Mn loadings) of –0.02, –0.07, –0.09, –0.07, and –0.08 eV/Mn atom for the MnO, $MnO_{1.5}$, MnO_2, $MnO_2H_{0.5}$, and MnO_2H phases, respectively, this difference is rather small and hence it is unlikely by itself to affect the ratio between the two crystal phases. Nonetheless, Mn might still favor the formation of one crystal phase over the other via purely structural effects, e.g., by modifying the fresh catalyst in such a way that it preferentially yields fcc or hcp upon reduction. Furthermore, it is worth noting that for the most stable phases and especially for the lowest loadings, Mn on the Co NPs is either more or roughly as stable than/as in bulk MnO, which was used in eq 6 as a reference state, underscoring the strong interactions between the metal and the promoter. This is in line with previous experimental studies that reported intimate contact between Mn and Co and corroborates the idea that (at least a portion of) Mn species will maintain stability and promotional activity over long periods under operation.

3.2. Structural Characterization of Mn@Co

In this section, we present a structural analysis of the GA trajectories, from which we excluded those candidates whose energies were larger then $E_{GM} + n_{Mn} \times 0.02$ eV, where E_{GM} is the energy of the GM and n_{Mn} is the number of Mn atoms. Reported error bars are the MADs with respect to the values averaged over the considered candidates.

In Figure 6, we report the surface coverage of the Co NPs with increasing Mn loading. We observe that, at a given Mn loading, the coverage is lower on the 6 nm fcc–Co NP than on the 8 nm fcc– and hcp–Co NPs, due to the higher surface-to-volume ratio in the former. Furthermore, while the coverage increases mostly linearly with the Mn:Co ratio on the 6 nm fcc–Co NP, on the other two slabs, it does so up to Mn:Co = 0.02–0.03, after which the curves start to plateau. This occurs due to the formation of sparse non-monolayer structures, which start to appear when the coverage reaches ∼80%. The Mn phase is shown to have a rather large effect on the coverage, with differences between highest and lowest coverages for a given NP and Mn loading that are often ∼20%. In particular, it is seen that coverage increases with the O:Mn ratio, due to oxygen atoms binding both to Mn and the Co surface, while it decreases with the O:H ratio, as hydroxyl groups often bind to Mn but not to the Co surface. We note that Johnson et al.[15] reported Co surface coverage measured via H_2 chemisorption of 10 and 40% for Mn:Co ratios of 0.01 and 0.05, respectively, which are lower than the values reported here. We attribute this discrepancy to the fact that, with increasing manganese loading, a significant portion of Mn ends up on the support, which implies that a nominal experimental Mn:Co ratio always corresponds to a larger one on our NP models.

Besides considering the overall Co surface coverage, it is insightful to investigate the preferential location of the promoter on the NPs. This is quantified in Figure 7, where we show the percentage of free Co sites with different coordination numbers (CN) for the investigated Mn phases on the 8 nm fcc– and hcp–Co NPs with increasing Mn loading. Data for the 6 nm

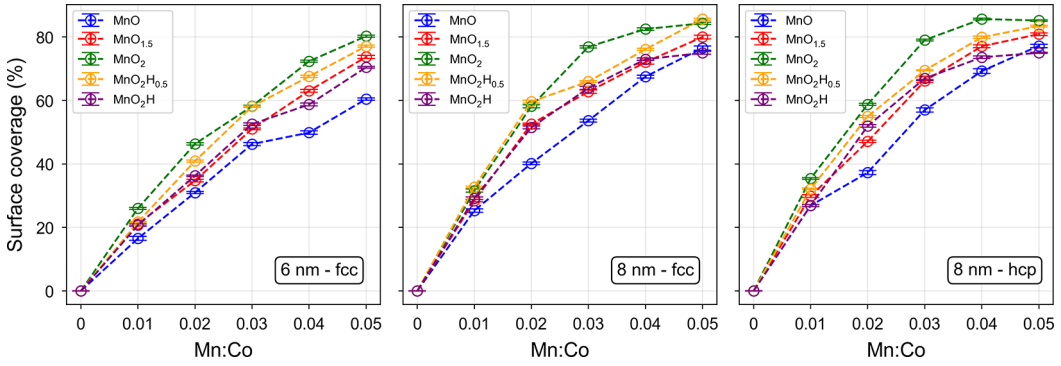

Figure 6. Surface coverage of the Co NP slabs with increasing Mn loading. Co–O and Co–Mn cutoffs of 2.15 and 3.0 Å, respectively, were employed to determine whether a Co atom was covered.

https://doi.org/10.1021/acscatal.6c04886
ACS Catal. XXXX, XXX, XXX–XXX

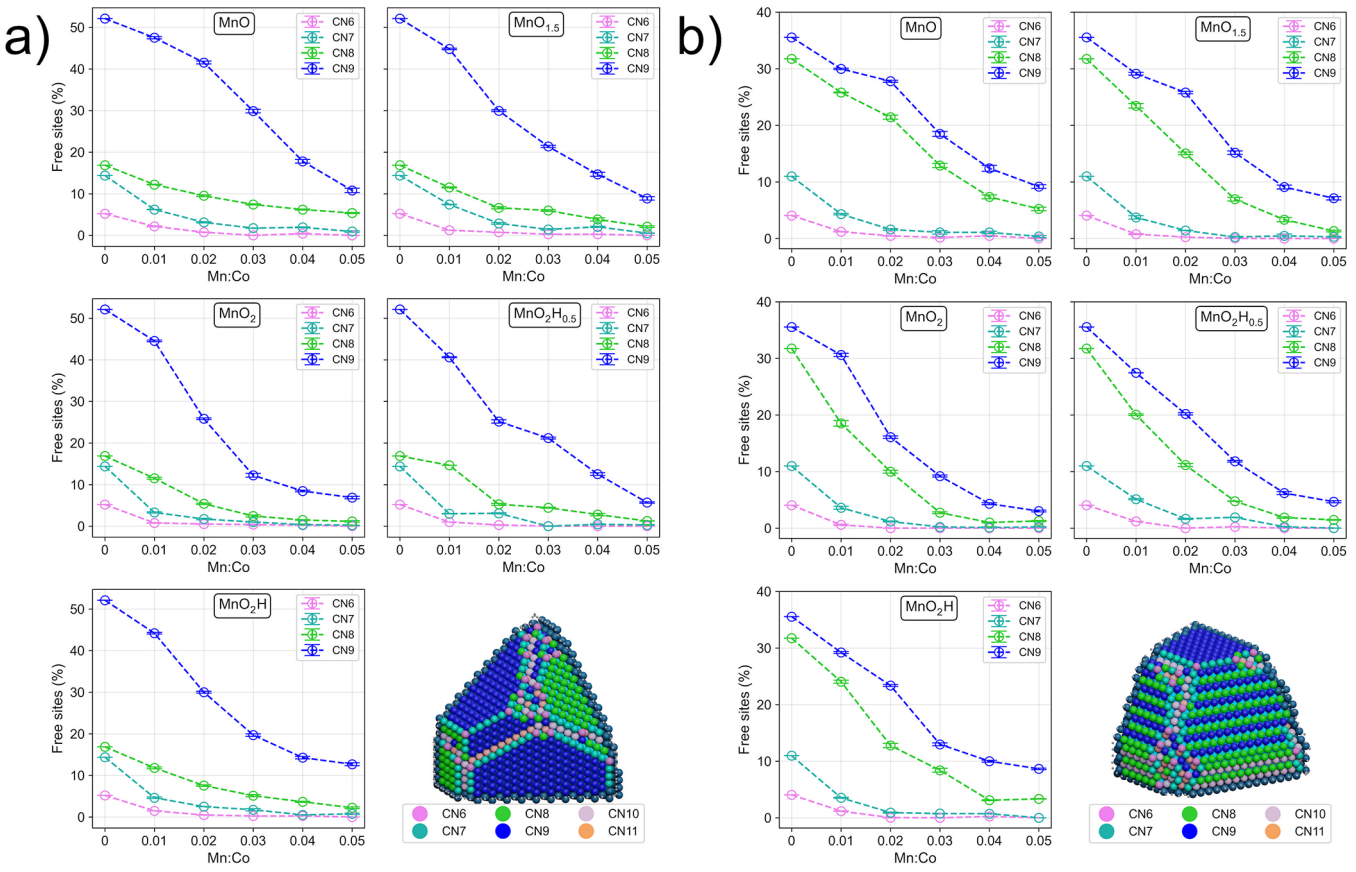

Figure 7. Percentage of free Co sites with different coordination numbers with increasing Mn:Co ratios for all the investigated Mn phases on the 8 nm fcc– (a) and hcp–Co (b) NPs.

fcc NP model are shown in Figure S14. As highlighted in the snapshot of the colored NP slabs in Figure 7, Co atoms with CN = 6 and 7 are found on the corners/kinks and on the edges/steps, respectively, while Co atoms with CN = 8 are predominantly found on the (100) terrace on the fcc model, while on the hcp NP, they are located on the (10–11) and (10–10) surfaces. Additionally, Co atoms with CN = 9 are found on the fcc(111), hcp(0001), and hcp(10–11) terraces. Free Co atoms with CN = 10 and 11, which are located at the base of step sites, diminish only slightly with increasing Mn loading since they are shielded by neighboring Co atoms and can hardly bind to Mn or O, or in fact any adsorbates relevant for FT synthesis, and were therefore not reported in the plots. Considering the fcc model, while the percentages of all the available Co sites decrease with Mn loading, this occurs disproportionately for the low-coordinated CN6 and CN7 sites, whose availability decreases sharply as soon as Mn is deposited on the particles and, already from low Mn:Co ratios, they are almost fully occupied, even though this effect is slightly less pronounced for the MnO and $MnO_{1.5}$ phases. On the other hand, we witness only a mild decrease of available CN8 and CN9 terrace atoms for Mn:Co = 0.01, and their significant coverage only takes place when the lower-coordinated atoms are nearly fully occupied. This indicates a clear preference for Mn to bind to the LCS on the Co NPs, which was already pointed out when discussing the GM structures presented in Figure 4. As mentioned in Section 3.1, this explains to a large extent the observed destabilization of Mn structures with increasing loading reported in Figure 5: Increasing loading forces Mn to populate the terraces, generating structures that are less stable, as the more favorable LCS are already occupied. These trends are also reproduced for the 6 nm fcc– and 8 nm hcp–Co models, even though the latter exposes more Co atoms with CN = 8 with respect to the fcc counterparts due to the fact that they are largely present, together with CN = 9 atoms, on the predominant (10–11) facets. Interestingly, on the hcp model, Mn binds preferentially to the CN = 8 atoms than to the CN = 9 ones. This is highlighted by the fact that, while the two sites are present in similar concentrations in the absence of Mn, as the promoter loading increases, the available CN = 8 Co atoms decrease significantly more. We ascribe this to the particularly favorable conformation for Mn adsorption on the hcp(10–10) facets, which are rich in CN = 8 atoms.

In Figures S15–S17, we report the Mn–Mn radial distribution function ($g(r)$) of all the Mn phases with increasing loading on the 6 and 8 nm fcc–Co and 8 nm hcp–Co slabs. For all distributions, we identify two peaks, one located roughly between 1.8 and 3.5 Å, which is relative to the first Mn–Mn coordination shell, and another, located between 4.0 and 6.5 Å, relative to the second Mn–Mn coordination shell. With increasing loading, we observe a sharp increase of both peaks, which indicate, as expected, Mn agglomeration. The first peak is, in all cases, significantly more intense than the second, which we link to the preference of Mn to form rather small islands lacking long-range order. This additionally underscores that, for these Mn:Co ratios, the formation of the Mn structures is mainly

https://doi.org/10.1021/acscatal.6c04886
ACS Catal. XXXX, XXX, XXX–XXX

governed by the Co NP surface conformation, as the energetic gain arising from binding to the most favorable Co sites overshadows the one coming from formation of bigger, crystalline-like, Mn conglomerates. Nevertheless, as shown in Table S2, the ratios between the areas under the first and second peaks consistently decrease with increasing Mn loading, indicating that further Mn addition might favor the formation of a more ordered overlayer encapsulating the Co NPs. There are no significant differences for the Mn–Mn $g(r)$ across the different Mn phases, indicating that they all form qualitatively similar structures. When considering the different slab models, we observe that the first and second peak intensities increase with Mn loading, which is less pronounced on the 6 nm fcc–Co NP as compared to the 8 nm fcc- and hcp–Co NPs, due to the fact that, given the larger surface area with respect to the number of Co atoms, on the former the same Mn loading results in a lower coverage. We note that the structural models discussed here do not consider the effect of the CO gas phase, which under FT conditions will influence Co particle shape[45] and might additionally cause a rearrangement of the promoter clusters. Even though this effect has not been directly investigated in the present study, in light of its strong binding, we expect CO to affect the promoter predominantly via competitive adsorption on the Co surface. In particular, it is likely that the weakly bound Mn structures located on the NP terraces will be displaced by CO upon exposure to the FT gas phase and might ultimately find an anchoring point by clustering with the strongly bound Mn species adsorbed on the Co LCS or by migrating to the Co–support interface.

3.3. Prediction of Mn Oxidation States

In our previous work,[46] we have compared the oxidation state of Mn against its atomic magnetic moments across a number of bulk Mn oxides and $Mn_xO_yH_z$ gas-phase clusters and found a strong quadratic correlation equal to (as calculated with the BEEF–vdW+U functional):

$$\mathrm{Magmom}_{\mathrm{Mn}} = -0.064\mathrm{OS}^2 - 0.313\mathrm{OS} + 5.310 \quad (7)$$

where $\mathrm{Magmom}_{\mathrm{Mn}}$ is the Mn atomic magnetic moment (in μ_B) and OS is the oxidation state. This was shown to hold true for qualitatively very different systems and to be more reliable than the correlation between Mn magnetic moments and Bader charge. Importantly, the experimentally measured oxidation state of Mn in Co FT catalysts does not per se inform us on the stoichiometry of the promoter, as the Co NPs can act as electron reservoirs and thus compensate the Mn electron donation to the O atoms. To clarify the Mn oxidation state–stoichiometry relationship, we have applied the correlation from our previous work to derive the average Mn oxidation state in the GM structures obtained in the GA runs, which are shown in Figure 8. This was possible because the employed fine-tuned CHGNet potential was also trained on the DFT-calculated atomic magnetic moments and can thus be used to make such predictions.

Strikingly, we observe that the Mn charge varies very little across the different phases, loadings, and slab models and is in all cases roughly 2+, despite the formal OS of the different investigated stoichiometries ranging between 2+ and 4+. This marked discrepancy can be explained, as previously postulated, by a charge compensation mechanism involving the Co surface, which partially oxidizes to keep Mn in the divalent state. Interestingly, this electronic effect might alter the reactivity of the Co atoms. This phenomenon has a strong self-regulating character, as it mostly does not play a role for the MnO phase, for which the predicted oxidation state largely aligns with the one expected based on the phase stoichiometry, while it becomes stronger with increasing O content. The observed remarkable inertia of the Mn atoms in respect to deviations from the divalent state can be rationalized based on the stability of the corresponding $[Ar]3d^5$ electronic configuration, where the maximum exchange among pairs of parallel-spin electrons significantly reduces the Coulombic potential energy, and which is also highlighted by the exceptionally high III ionization energy of Mn.[81] Simply put, when the Mn cluster stoichiometry would require a Mn oxidation state >2, the O (or OH) ligands draw charge from the Co surface instead, so that the favorable Mn^{2+} electronic configuration is preserved. Nonetheless, this behavior is likely characteristic of the structures predicted here consisting of monolayer patches of Mn (hydro)oxide on the Co surface, while the correspondence between Mn stoichiometry and oxidation state will become more direct when larger, bulk-like configurations start to appear. We note that the results reported here are in line with

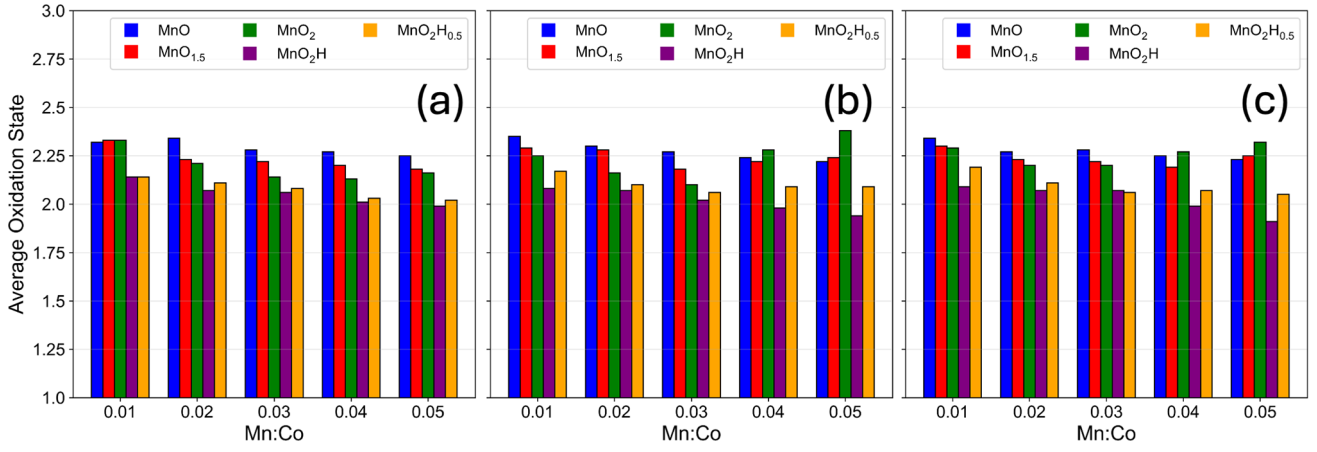

Figure 8. Predicted average oxidation state of Mn in the different phases with increasing loading on the (a) 6 nm fcc–Co, (b) 8 nm fcc–Co, and (c) 8 nm hcp–Co nanoparticles.

https://doi.org/10.1021/acscatal.6c04886
ACS Catal. XXXX, XXX, XXX–XXX

experimental studies that observed mostly divalent Mn both in the activated state and under FT conditions,[15,17,18] but we also point out that hardly any conclusion (besides that no bulk Mn oxides higher than MnO are formed) can be made regarding the structure of Mn just based on the experimentally measured oxidation state, as our study shows that this is not directly related to the actual stoichiometry of the promoter on the Co NPs.

Last, we note that the predicted oxidation states of Mn in the different support structures reported in Table S1 match closely those expected based on stoichiometry on the non-reducible γ-Al_2O_3 and α-SiO_2 oxides, while the two quantities diverge for most structures on TiO_2, where Mn retains the 2+ regardless of the cluster stoichiometry, similarly to what was observed for Mn on Co. We further observe that the most stable structures on both γ-Al_2O_3 and α-SiO_2 are those where Mn is found in the divalent state, highlighting the higher stability of this electronic configuration.

4. CONCLUSIONS

The combination of computational techniques employed in this work enabled us to sketch a holistic picture of the structure of Mn-promoted Co catalysts. Our calculations show that, on average, Mn is strongly anchored to Co surfaces, suggesting that the promoter retains its structure over long operational times and consistent with the widely reported intimate Co–Mn contact observed experimentally.

We achieved good agreement with experiments in the prediction of Mn oxidation states, which were found to be close to 2+ regardless of promoter stoichiometry, loading, crystal phase, or particle size. Furthermore, the predicted weakening of Mn binding with increasing loading explains the experimentally observed saturation of Co surface coverage upon Mn addition, indicating the formation of Co-independent promoter structures on the support. This behavior stems from the fact that not all Mn species are equivalent: Mn preferentially binds to LCS on the NP surface, but once these are occupied, it populates terrace sites where it is less stable and might be more prone to removal.

Given the pivotal role of LCS in enabling CO dissociation on unpromoted Co catalysts, our results strongly indicate that Mn–LCS interactions are a key aspect of the promotional mechanism. In particular, experimental evidence indicating that Mn increases CO dissociation rates[15,17,31] suggests that the effect of the promoter is not limited to simply blocking the LCS. A possible promotional mechanism is one in which, being located on the stepped areas on the NPs, Mn is blocking a portion of the LCS but promoting the adjacent ones, causing a net increase in reaction rate. Alternatively, if Mn was fully blocking the LCS, the increased TOF could be explained by the promotion of the neighboring terrace sites. Both scenarios imply, as previously postulated, that there is a tradeoff between the promotional effect achieved by adding Mn and the blocking of the Co surface sites, which explains the widely observed maxima in reaction rate with Mn loading. Even though we did not investigate the specifics of the electronic promotional mechanism, the fact that different Mn phases are often close in energy (Figure 5) suggests that O and OH ligands can readily rearrange under Fischer–Tropsch conditions, which might facilitate CO dissociation through vacancy formation–filling cycles and oxygen removal processes. Overall, resolving how the interactions between Mn and the Co LCS affect the reaction network will be crucial to fully understand the mechanism through which the promoter alters the reaction network, not only because of the pivotal role of these sites in the unpromoted catalysts but also because the Mn species located on the LCS are more likely to retain stability over long reaction periods due to their strong anchoring.

Besides affecting the FT reaction, the interactions between Mn and the Co LCS might additionally increase catalyst stability by lowering sintering rates. Sintering via Ostwald ripening is a prominent deactivation mechanism for FT Co catalysts, which is believed to occur via highly mobile Co subcarbonyl species.[82−85] These preferentially form from the LCS, which are the weakly bound metal atoms on the Co surface and thus more susceptible to detachment. By binding/covering the LCS, Mn would likely hinder the formation of the subcarbonyl species with consequent reduction of sintering rates. This is in line with previous reports of increased catalyst resistance upon Mn promotion.[78,86]

To conclude, we have leveraged the exceptional computational speed-up delivered by MLPs in a GA where Mn structures are optimized on realistic Co NP models produced via our recently published DFT-based MC approach. By considering large NP models instead of periodic surfaces, we were able to embrace the complexity of real catalytic systems, considering the effects of particle size, crystal phase and Mn loading. We point out that we neglected possible Co surface reconstruction induced by Mn as well as the effect of CO, which might alter the Mn structures calculated here. Additionally, we did not characterize Mn species that form at the Co-support interface, which might contribute to the promotional effect. Another limitation of this work is related to the fact that we optimized Mn phases of fixed stoichiometries that do not necessarily reflect the most favorable O and H contents, which in the real catalyst are achieved via dynamic adsorption and desorption of H_2 and H_2O. We note that this shortcoming could be overcome in future works by employing a recently developed grand canonical implementation of the GA.[87] Despite this, we believe that the gap between technical catalysts and our models is drastically smaller in respect to the state of the art and argue that our work significantly advances the current understanding of Mn promotion of Co FT catalysts.

■ ASSOCIATED CONTENT

Data Availability Statement

Genetic algorithm scripts, fine-tuned CHGNet in .tar format, global minima structures in .xyz format, plots (.png) showing algorithm progression (Energy vs # of candidates), database files in .db format containing all relaxed candidates for all genetic algorithm runs, training dataset in both .db and .json formats, and structural files of the $Mn_xO_yH_z$ motifs on different fcc–Co surface conformations extracted from global minima structures can be found at our kitopen repository (10.35097/njvtj906ggr9arf8).

Supporting Information

The Supporting Information is available free of charge at https://pubs.acs.org/doi/10.1021/acscatal.6c04886.

Snapshots of five sample database structures, DFT-tuned CHGNet parity plots for $Mn_xO_yH_z$@hcp Co structures, plot showing employed thermal corrections for adsorbed O and OH groups, phase diagrams at reduction conditions, snapshots and energies of the fine-tuned

https://doi.org/10.1021/acscatal.6c04886
ACS Catal. XXXX, XXX, XXX−XXX

CHGNet-relaxed $Mn_xO_yH_z$ motifs on different fcc–Co surface conformations extracted from global minima structures, snapshots and table including specifications of the DFT-calculated Mn structures calculated on the different supports, site titration plots for the 6 nm fcc–Co NP slab, and Mn–Mn radial distribution functions (PDF)

Coordinates in xyz format of the DFT-calculated Mn structures on the different supports (TXT)

AUTHOR INFORMATION

Corresponding Author

Felix Studt – *Institute of Catalysis Research and Technology, Karlsruhe Institute of Technology, Hermann-von-Helmholtz-Platz 1, Eggenstein-Leopoldshafen 76344, Germany; Institute for Chemical Technology and Polymer Chemistry, Karlsruhe Institute of Technology, Engesserstr. 20, Karlsruhe 76131, Germany;* orcid.org/0000-0001-6841-4232; Email: felix.studt@kit.edu

Authors

Enrico Sireci – *Institute of Catalysis Research and Technology, Karlsruhe Institute of Technology, Hermann-von-Helmholtz-Platz 1, Eggenstein-Leopoldshafen 76344, Germany;* orcid.org/0000-0002-3253-6518

Julie-Ann Hoffman – *Catalysis Institute, Department of Chemical Engineering, University of Cape Town (UCT), Cape Town 7701, South Africa;* orcid.org/0000-0002-5717-658X

Dmitry I. Sharapa – *Institute of Catalysis Research and Technology, Karlsruhe Institute of Technology, Hermann-von-Helmholtz-Platz 1, Eggenstein-Leopoldshafen 76344, Germany*

Thobani G. Gambu – *Catalysis Institute, Department of Chemical Engineering, University of Cape Town (UCT), Cape Town 7701, South Africa;* orcid.org/0000-0002-6551-9220

Eric van Steen – *Catalysis Institute, Department of Chemical Engineering, University of Cape Town (UCT), Cape Town 7701, South Africa;* orcid.org/0000-0003-4659-8522

Complete contact information is available at: https://pubs.acs.org/doi/10.1021/acscatal.6c04886

Notes

The authors declare no competing financial interest.

ACKNOWLEDGMENTS

We gratefully acknowledge that this study is supported by the German Federal Ministry of Research, Technology and Space (BMFTR), within the CARE-O-SENE project (03SF0673). The authors thank the Council for Scientific and Industrial Research's (CSIR's) Centre for High Performance Computing (CHPC) and the University of Cape Town's ICTS High Performance Computing team, http://hpc.uct.ac.za/. The University of Cape Town gratefully acknowledges the financial support of the National Research Foundation (NRF) and DSI-NRF SARChI (UID: 114606). The authors acknowledge support by the state of Baden-Württemberg through bwHPC and the German Research Foundation (DFG) through grant no. INST 40/575-1 FUGG (JUSTUS 2 cluster, RVs bw17D011). Support from the Helmholtz Association is also gratefully acknowledged.

REFERENCES

(1) de Klerk, A.; Chauhan, G.; Halmenschlager, C.; Link, F.; Montoya Sánchez, N.; Gartley, B.; El-Sayed, H. E. M.; Sehdev, R.; Lehoux, R. Sustainable Aviation Fuel: Pathways to Fully Formulated Synthetic Jet Fuel via Fischer–Tropsch Synthesis. *Energy Sci. Eng.* **2024**, *12* (2), 394–409.

(2) Montoya Sánchez, N.; Link, F.; Chauhan, G.; Halmenschlager, C.; El-Sayed, H. E. M.; Sehdev, R.; Lehoux, R.; de Klerk, A. Conversion of Waste to Sustainable Aviation Fuel via Fischer–Tropsch Synthesis: Front-End Design Decisions. *Energy Sci. Eng.* **2022**, *10* (5), 1763–1789.

(3) Li, A.; Zheng, J.; Wang, Z.; Zhang, Z. Research Advances and Future Perspectives in Fischer–Tropsch Synthesis for Sustainable Aviation Fuel. *Sustainable Energy Fuels* **2025**, *10*, 42–55.

(4) Moodley, D.; Botha, T.; Crous, R.; Potgieter, J.; Visagie, J.; Walmsley, R.; Dwyer, C. Catalysis for Sustainable Aviation Fuels: Focus on Fischer-Tropsch Catalysis. In *Catalysis for a Sustainable Environment*; Wiley, **2024**, pp 73–116.

(5) Saeys, M. Two Diverging Paths for Clean Fuel. *Science* **2025**, *390*, 443.

(6) Datye, A. K.; Niemantsverdriet, H.; van Bavel, A. P.; Robota, H.; Moodley, D.; Steynberg, A. P.; Li, Y.-W.; Schrader, L. On to the next Century of Fischer–Tropsch Synthesis. *Nat. Chem. Eng.* **2025**, *2* (12), 719–723.

(7) Sun, B.; Xu, K.; Nguyen, L.; Qiao, M.; Tao, F. F. Preparation and Catalysis of Carbon-Supported Iron Catalysts for Fischer-Tropsch Synthesis. *ChemCatChem* **2012**, *4*, 1498–1511.

(8) Davis, B. H. Fischer-Tropsch Synthesis: Reaction Mechanisms for Iron Catalysts. *Catal. Today* **2009**, *141* (1–2), 25–33.

(9) Iglesia, E. Design, Synthesis, and Use of Cobalt-Based Fischer-Tropsch Synthesis Catalysts. *Appl. Catal. A* **1997**, *161*, 59–78.

(10) Khodakov, A. Y.; Chu, W.; Fongarland, P. Advances in the Development of Novel Cobalt Fischer-Tropsch Catalysts for Synthesis of Long-Chain Hydrocarbons and Clean Fuels. *Chem. Rev.* **2007**, *107* (5), 1692–1744.

(11) Arsalanfar, M.; Mirzaei, A. A.; Bozorgzadeh, H. R.; Samimi, A. A Review of Fischer-Tropsch Synthesis on the Cobalt Based Catalysts. *Phys. Chem. Res.* **2014**, *2* (2), 179–201.

(12) Davis, B. H. Fischer-Tropsch Synthesis: Comparison of Performances of Iron and Cobalt Catalysts. *Ind. Eng. Chem. Res.* **2007**, *46* (26), 8938–8945.

(13) Zimina, A.; Fadlalla, M. I.; Potgieter, J.; Jimenez, C. E.; Ilica, R.; Sireci, E.; Sharapa, D. I.; de Oliveira, D.; Hsu, C.; Saraci, E.; Wolf, M.; Sakoglu, P.; Skaltsogiannis, A.; Zhong, T.; Bär, M.; Botha, T.; Moodley, D.; Claeys, M.; Studt, F.; Grunwaldt, J.-D. Comparison of Industrially Relevant Fischer–Tropsch Cobalt Catalysts Supported on Alumina and Modified Silica with Complementary *In Situ* and *Operando* Characterization Methods. *J. Phys. Chem. C* **2026**, *130* (10), 3676–3690.

(14) Tucker, C. L.; Ragoo, Y.; Mathe, S.; Macheli, L.; Bordoloi, A.; Rocha, T. C. R.; Govender, S.; Kooyman, P. J.; van Steen, E. Manganese Promotion of a Cobalt Fischer-Tropsch Catalyst to Improve Operation at High Conversion. *J. Catal.* **2022**, *411*, 97–108.

(15) Johnson, G. R.; Werner, S.; Bell, A. T. An Investigation into the Effects of Mn Promotion on the Activity and Selectivity of Co/SiO_2 for Fischer-Tropsch Synthesis: Evidence for Enhanced CO Adsorption and Dissociation. *ACS Catal.* **2015**, *5* (10), 5888–5903.

(16) Gupta, S. S.; Shenai, P. M.; Meeuwissen, J.; Bezemer, G. L.; Shetty, S. Electronic Promotion Effects of Metal Oxides: A Case Study of MnO Impact on Fischer-Tropsch Catalysis. *J. Phys. Chem. C* **2021**, *125* (39), 21390–21401.

(17) Kimpel, T. F.; Liu, J. X.; Chen, W.; Pestman, R.; Hensen, E. J. M. Pressure Dependence and Mechanism of Mn Promotion of Silica-Supported Co Catalyst in the Fischer-Tropsch Reaction. *J. Catal.* **2023**, *425*, 181–195.

(18) Morales, F.; De Groot, F. M. F.; Gijzeman, O. L. J.; Mens, A.; Stephan, O.; Weckhuysen, B. M. Mn Promotion Effects in Co/TiO_2 Fischer-Tropsch Catalysts as Investigated by XPS and STEM-EELS. *J. Catal.* **2005**, *230* (2), 301–308.
(19) Vasiliades, M. A.; Moodley, D.; Crous, R.; Potgieter, J.; Botha, T.; Efstathiou, A. M. Influence of the Mn Promoter on the Composition and Activity of the Adsorbed Phase in the Carbon Paths of the CO Hydrogenation Reaction on 20 wt % Co/MnO_x-Al_2O_3: An Operando-SSITKA and Transient Kinetic Study. *ACS Catal.* **2025**, *15* (7), 5318–5338.
(20) Potgieter, J. H.; Moodley, D.; Botha, T.; Visagie, J.; Manong, T.; Frank, M.; Claeys, M.; van Steen, E.; Böltken, T.; Pfeifer, P. Development of Promoted Cobalt/Alumina Fischer-Tropsch Catalysts for Increased Activity and Selectivity: Micro-Reactor to Piloting Scale. *Catal. Today* **2024**, *432*, 114554.
(21) Johnson, G. R.; Werner, S.; Bustillo, K. C.; Ercius, P.; Kisielowski, C.; Bell, A. T. Investigations of Element Spatial Correlation in Mn-Promoted Co-Based Fischer-Tropsch Synthesis Catalysts. *J. Catal.* **2015**, *328*, 111–122.
(22) Pedersen, E. Ø.; Svenum, I. H.; Blekkan, E. A. Mn Promoted Co Catalysts for Fischer-Tropsch Production of Light Olefins – An Experimental and Theoretical Study. *J. Catal.* **2018**, *361*, 23–32.
(23) Bezemer, G. L.; Radstake, P. B.; Falke, U.; Oosterbeek, H.; Kuipers, H. P. C. E.; Van Dillen, A. J.; De Jong, K. P. Investigation of Promoter Effects of Manganese Oxide on Carbon Nanofiber-Supported Cobalt Catalysts for Fischer-Tropsch Synthesis. *J. Catal.* **2006**, *237* (1), 152–161.
(24) Morales, F.; de Smit, E.; de Groot, F. M. F.; Visser, T.; Weckhuysen, B. M. Effects of Manganese Oxide Promoter on the CO and H_2 Adsorption Properties of Titania-Supported Cobalt Fischer-Tropsch Catalysts. *J. Catal.* **2007**, *246* (1), 91–99.
(25) Dinse, A.; Aigner, M.; Ulbrich, M.; Johnson, G. R.; Bell, A. T. Effects of Mn Promotion on the Activity and Selectivity of Co/SiO_2 for Fischer-Tropsch Synthesis. *J. Catal.* **2012**, *288*, 104–114.
(26) Den Breejen, J. P.; Frey, A. M.; Yang, J.; Holmen, A.; Van Schooneveld, M. M.; De Groot, F. M. F.; Stephan, O.; Bitter, J. H.; De Jong, K. P. A Highly Active and Selective Manganese Oxide Promoted Cobalt-on-Silica Fischer-Tropsch Catalyst. *Top. Catal.* **2011**, *54* (13–15), 768–777.
(27) Vermaak, V.; Cunningham, R. D.; Potgieter, J. H.; Botha, J. M.; van Steen, E.; Claeys, M.; Fadlalla, M.; Hoffman, J.-A.; Abdullah, S.; Sireci, E.; Studt, F.; Zimina, A.; Grunwaldt, J.-D.; Hsu, C.; Wolf, M.; Jiménez, C.; Sakoglu, P.; Moodley, D. Manganese-Enhanced Cobalt Catalysts for Fischer-Tropsch Synthesis: A Review of Structural and Electronic Promotion Effects. *Catal. Sci. Technol.* **2026**, *16* (5), 1488–1530.
(28) Liang, Q.; Chen, K.; Hou, W.; Yan, Q. CO Hydrogenation over Nanometer Spinel-Type Co/Mn Complex Oxides Prepared by Sol-Gel Method. *Appl. Catal. A* **1998**, *166*, 191–199.
(29) Farooq, D.; Costley-Wood, L.; Stockenhuber, S.; Vamvakeros, A.; Price, S. W. T.; Allen, L. J.; Drnec, J.; Paterson, J.; Peacock, M.; Irving, D. J. M.; Chater, P. A.; Beale, A. M. Mn-Promoted Co/TiO_2 Catalysts: Quantitative Analysis of Cobalt Polymorphs and Stacking Faults and Its Effect on Fischer-Tropsch Synthesis Performance. *ACS Catal.* **2026**, *16* (4), 3296–3306.
(30) Werner, S.; Johnson, G. R.; Bell, A. T. Synthesis and Characterization of Supported Cobalt-Manganese Nanoparticles as Model Catalysts for Fischer-Tropsch Synthesis. *ChemCatChem* **2014**, *6* (10), 2881–2888.
(31) Ivanez, O.; Blekkan, E. A. Study of the Role of the Support Material in the Manganese Promotion of Cobalt-Based Fischer-Tropsch Synthesis Catalysts. *Appl. Catal. A* **2025**, *708*, No. 120611.
(32) Chen, H.; Lian, Z.; Zhao, X.; Wan, J.; Pieters, P. F.; Oliver-Meseguer, J.; Yang, J.; Pach, E.; Carenco, S.; Treps, L.; Liakakos, N.; Shan, Y.; Altoe, V.; Wong, E.; Zhuo, Z.; Yang, F.; Su, J.; Guo, J.; Blum, M.; H. Lapidus, S.; Hunt, A.; Waluyo, I.; Ogasawara, H.; Zheng, H.; Yang, P.; Bell, A. T.; López, N.; Salmeron, M. The Role of Manganese in $CoMnO_x$ Catalysts for Selective Long-Chain Hydrocarbon Production via Fischer-Tropsch Synthesis. *Nat. Commun.* **2024**, *15* (1), 10294.
(33) Zhang, M.; Chi, S.; Huang, H.; Yu, Y. Mechanism Insight into MnO for CO Activation and O Removal Processes on Co(0001) Surface: A DFT and KMC Study. *Appl. Surf. Sci.* **2021**, *567*, 150854.
(34) Ciufo, R. A.; Han, S.; Floto, M. E.; Henkelman, G.; Mullins, C. B. Low Temperature Dissociation of CO on Manganese Promoted Cobalt(Poly). *Chem. Commun.* **2020**, *56* (19), 2865–2868.
(35) Morales, F.; De Groot, F. M. F.; Glatzel, P.; Kleimenov, E.; Bluhm, H.; Hävecker, M.; Knop-Gericke, A.; Weckhuysen, B. M. In Situ X-Ray Absorption of $Co/Mn/TiO_2$ Catalysts for Fischer-Tropsch Synthesis. *J. Phys. Chem. B* **2004**, *108* (41), 16201–16207.
(36) Petersen, M. A.; Van Den Berg, J. A.; Ciobîcâ, I. M.; Van Helden, P. Revisiting CO Activation on Co Catalysts: Impact of Step and Kink Sites from DFT. *ACS Catal.* **2017**, *7* (3), 1984–1992.
(37) Liu, J. X.; Su, H. Y.; Sun, D. P.; Zhang, B. Y.; Li, W. X. Crystallographic Dependence of CO Activation on Cobalt Catalysts: HCP vs FCC. *J. Am. Chem. Soc.* **2013**, *135* (44), 16284–16287.
(38) Chen, W.; Zijlstra, B.; Filot, I. A. W.; Pestman, R.; Hensen, E. J. M. Mechanism of Carbon Monoxide Dissociation on a Cobalt Fischer–Tropsch Catalyst. *ChemCatChem* **2018**, *10* (1), 136–140.
(39) Zijlstra, B.; Broos, R. J. P.; Chen, W.; Bezemer, G. L.; Filot, I. A. W.; Hensen, E. J. M. The Vital Role of Step-Edge Sites for Both CO Activation and Chain Growth on Cobalt Fischer-Tropsch Catalysts Revealed through First-Principles-Based Microkinetic Modeling Including Lateral Interactions. *ACS Catal.* **2020**, *10* (16), 9376–9400.
(40) Rommens, K. T.; Saeys, M. Molecular Views on Fischer-Tropsch Synthesis. *Chem. Rev.* **2023**, *123* (9), 5798–5858.
(41) Banerjee, A.; Van Bavel, A. P.; Kuipers, H. P. C. E.; Saeys, M. CO Activation on Realistic Cobalt Surfaces: Kinetic Role of Hydrogen. *ACS Catal.* **2017**, *7* (8), 5289–5293.
(42) Böller, B.; Durner, K. M.; Wintterlin, J. The Active Sites of a Working Fischer–Tropsch Catalyst Revealed by Operando Scanning Tunnelling Microscopy. *Nat. Catal.* **2019**, *2* (11), 1027–1034.
(43) Sireci, E.; Sharapa, D. I.; Studt, F. A Comprehensive Overview of Active Sites of Fcc-Co Nanoparticles and Their Role in CO Splitting—A DFT Study. *J. Phys. Chem. C* **2025**, *129* (49), 21634–21641.
(44) Sireci, E.; Grüger, T. D.; Plessow, P. N.; Sharapa, D. I.; Studt, F. Modeling the Shape and Stability of Co Nanoparticles as a Function of Size and Support Interactions through DFT Calculations and Monte Carlo Simulations. *J. Phys. Chem. C* **2025**, *129* (29), 13232–13243.
(45) Sireci, E.; Grüger, T. D.; Plessow, P. N.; Sharapa, D. I.; Studt, F. Modeling the Shape and Stability of Supported Co Nanoparticles under Fischer-Tropsch Conditions via DFT Calculations and Monte Carlo Simulations: Insights into CO-Driven Surface Reconstruction. *Catal. Sci. Technol.* **2025**, *15* (22), 6703–6715.
(46) Hoffman, J.-A.; Sireci, E.; Gambu, T. G.; Sharapa, D.; Studt, F.; van Steen, E. Bridging Calculated Charges and Formal Oxidation State of Manganese Oxides: A DFT/DFT+U Study. *Phys. Chem. Chem. Phys.* **2026**, *28* (27),17025–17033.
(47) Deng, B.; Zhong, P.; Jun, K. J.; Riebesell, J.; Han, K.; Bartel, C. J.; Ceder, G. CHGNet as a Pretrained Universal Neural Network Potential for Charge-Informed Atomistic Modelling. *Nat. Mach. Intell.* **2023**, *5* (9), 1031–1041.
(48) Klumpers, B.; Hensen, E. J. M.; Filot, I. A. W. Transferable, Living Data Sets for Predicting Global Minimum Energy Nanocluster Geometries. *J. Chem. Theory Comput.* **2024**, *20* (15), 6801–6812.
(49) Sun, G.; Sautet, P. Metastable Structures in Cluster Catalysis from First-Principles: Structural Ensemble in Reaction Conditions and Metastability Triggered Reactivity. *J. Am. Chem. Soc.* **2018**, *140* (8), 2812–2820.
(50) Cannizzaro, F.; Klumpers, B.; Filot, I. A. W.; Hensen, E. J. M. Microkinetics of CO_2 Hydrogenation to Methanol on In_2O_3-Supported Ni-In Clusters. *Appl. Catal. B* **2026**, *384*, 126238.
(51) Van de Loosdrecht, J.; Botes, F. G.; Ciobîcă, I. M.; Ferreira, A.; Gibson, P.; Moodley, D. J.; Saib, A. M.; Visagie, J. L.; Weststrate, C. J.; Niemantsverdriet, J. W. Fischer-Tropsch Synthesis: Catalysts and Chemistry. *Compr. Inorg. Chem. II* **2013**, *7*, 525–557.
(52) Van Steen, E.; Claeys, M.; Dry, M. E.; Van De Loosdrecht, J.; Viljoen, E. L.; Visagie, J. L. Stability of Nanocrystals: Thermodynamic

Analysis of Oxidation and Re-Reduction of Cobalt in Water/Hydrogen Mixtures. *J. Phys. Chem. B* **2005**, *109* (8), 3575–3577.
(53) Wolf, M.; Fischer, N.; Claeys, M. Formation of Metal-Support Compounds in Cobalt-Based Fischer-Tropsch Synthesis: A Review. *Chem Catal.* **2021**, *1* (5), 1014–1041.
(54) Wolf, M.; Fischer, N.; Claeys, M. Water-Induced Deactivation of Cobalt-Based Fischer–Tropsch Catalysts. *Nat. Catal.* **2020**, *3* (12), 962–965.
(55) Den Breejen, J. P.; Radstake, P. B.; Bezemer, G. L.; Bitter, J. H.; Frøseth, V.; Holmen, A; De Jong, K. P. On the Origin of the Cobalt Particle Size Effects in Fischer-Tropsch Catalysis. *J. Am. Chem. Soc.* **2009**, *131* (20), 7197–7203.
(56) Bezemer, G. L.; Bitter, J. H.; Kuipers, H. P. C. E.; Oosterbeek, H.; Holewijn, J. E.; Xu, X.; Kapteijn, F.; Van Diilen, A. J.; De Jong, K. P. Cobalt Particle Size Effects in the Fischer-Tropsch Reaction Studied with Carbon Nanofiber Supported Catalysts. *J. Am. Chem. Soc.* **2006**, *128* (12), 3956–3964.
(57) Prieto, G.; Martínez, A.; Concepción, P.; Moreno-Tost, R. Cobalt Particle Size Effects in Fischer-Tropsch Synthesis: Structural and in Situ Spectroscopic Characterisation on Reverse Micelle-Synthesised Co/ITQ-2 Model Catalysts. *J. Catal.* **2009**, *266* (1), 129–144.
(58) Vilhelmsen, L. B.; Hammer, B. Systematic Study of Au 6 to Au 12 Gold Clusters on MgO(100) F Centers Using Density-Functional Theory. *Phys. Rev. Lett.* **2012**, *108* (12), 126101.
(59) Vilhelmsen, L. B.; Hammer, B. A Genetic Algorithm for First Principles Global Structure Optimization of Supported Nano Structures. *J. Chem. Phys.* **2014**, *141* (4), 044711.
(60) Liu, C.; Uslamin, E. A.; Khramenkova, E.; Sireci, E.; Ouwehand, L. T. L. J.; Ganapathy, S.; Kapteijn, F.; Pidko, E. A. High Stability of Methanol to Aromatic Conversion over Bimetallic Ca,Ga-Modified ZSM-5. *ACS Catal.* **2022**, *12* (5), 3189–3200.
(61) Khramenkova, E. V.; Venkatraman, H.; Soethout, V.; Pidko, E. A. Global Optimization of Extraframework Ensembles in Zeolites: Structural Analysis of Extraframework Aluminum Species in MOR and MFI Zeolites. *Phys. Chem. Chem. Phys.* **2022**, *24* (44), 27047–27054.
(62) Kresse, G.; Hafner, J. Ab Initio Molecular Dynamics for Liquid Metals. *Phys. Rev. B* **1993**, *47* (1), 558–561.
(63) Kresse, G.; Furthmüller, J. Efficiency of Ab-Initio Total Energy Calculations for Metals and Semiconductors Using a Plane-Wave Basis Set. *Comput. Mater. Sci.* **1996**, *6*, 15–50.
(64) Wellendorff, J.; Lundgaard, K. T.; Møgelhøj, A.; Petzold, V.; Landis, D. D.; Nørskov, J. K.; Bligaard, T.; Jacobsen, K. W. Density Functionals for Surface Science: Exchange-Correlation Model Development with Bayesian Error Estimation. *Phys. Rev. B Condens. Matter Mater. Phys.* **2012**, *85* (23), 235149.
(65) Kresse, G.; Joubert, D. From Ultrasoft Pseudopotentials to the Projector Augmented-Wave Method. *Phys. Rev. B* **1999**, *59* (3), 1758–1775.
(66) Dudarev, S. L.; Botton, G. A.; Savrasov, S. Y.; Humphreys, C. J.; Sutton, A. P. Electron-Energy-Loss Spectra and the Structural Stability of Nickel Oxide: An LSDAU Study. *Phys. Rev. B* **1998**, *57* (3), 1505–1509.
(67) Deaven, D. M.; Ho, K. M. Molecular Geometry Optimization with a Genetic Algorithm. *Phys. Rev. Lett.* **1995**, *75* (2), 288–291.
(68) Lloyd, L. D.; Johnston, R. L.; Salhi, S. Strategies for Increasing the Efficiency of a Genetic Algorithm for the Structural Optimization of Nanoalloy Clusters. *J. Comput. Chem.* **2005**, *26* (10), 1069–1078.
(69) Johnston, R. L. Evolving Better Nanoparticles: Genetic Algorithms for Optimising Cluster Geometries. *Dalton Trans.* **2003**, *32* (22), 4193–4207.
(70) Kuryla, D.; Berger, F.; Csányi, G.; Michaelides, A. How Accurate Are DFT Forces? Unexpectedly Large Uncertainties in Molecular Datasets. *J. Chem. Phys.* **2025**, *163*, 224313.
(71) Kovács, D. P.; Moore, J. H.; Browning, N. J.; Batatia, I.; Horton, J. T.; Pu, Y.; Kapil, V.; Witt, W. C.; Magdău, I. B.; Cole, D. J.; Csányi, G. MACE-OFF: Short-Range Transferable Machine Learning Force Fields for Organic Molecules. *J. Am. Chem. Soc.* **2025**, *147* (21), 17598–17611.
(72) Perego, S.; Purcel, M.; Baum, Y.; Chen, S.; Müller, A. S.; Parrinello, M.; Behrens, M.; Muhler, M.; Bonati, L. No Time for Nitrides: How Cobalt Alloying Promotes Iron Catalysts for Ammonia Decomposition. *ACS Catal.* **2025**, *15*, 16690–16702.
(73) Perego, S.; Bonati, L.; Tripathi, S.; Parrinello, M. How Dynamics Changes Ammonia Cracking on Iron Surfaces. *ACS Catal.* **2024**, *14* (19), 14652–14664.
(74) Levine, D. S.; Shuaibi, M.; Spotte-Smith, E. W. C.; Taylor, M. G.; Hasyim, M. R.; Michel, K.; Batatia, I.; Csányi, G.; Dzamba, M.; Eastman, P.; Frey, N. C.; Fu, X.; Gharakhanyan, V.; Krishnapriyan, A. S.; Rackers, J. A.; Raja, S.; Rizvi, A.; Rosen, A. S.; Ulissi, Z.; Vargas, S.; Zitnick, C. L.; Blau, S. M.; Wood, B. M. *The Open Molecules 2025 (OMol25) Dataset, Evaluations, and Models*; **2025**. http://arxiv.org/abs/2505.08762.
(75) Batatia, I.; Benner, P.; Chiang, Y.; Elena, A. M.; Kovács, D. P.; Riebesell, J.; Advincula, X. R.; Asta, M.; Avaylon, M.; Baldwin, W. J.; Berger, F.; Bernstein, N.; Bhowmik, A.; Bigi, F.; Blau, S. M.; Cărare, V.; Ceriotti, M.; Chong, S.; Darby, J. P.; De, S.; Della Pia, F.; Deringer, V. L.; Elijošius, R.; El-Machachi, Z.; Fako, E.; Falcioni, F.; Ferrari, A. C.; Gardner, J. L. A.; Gawkowski, M. J.; Genreith-Schriever, A.; George, J.; Goodall, R. E. A.; Grandel, J.; Grey, C. P.; Grigorev, P.; Han, S.; Handley, W.; Heenen, H. H.; Hermansson, K.; Ho, C. H.; Hofmann, S.; Holm, C.; Jaafar, J.; Jakob, K. S.; Jung, H.; Kapil, V.; Kaplan, A. D.; Karimitari, N.; Kermode, J. R.; Kourtis, P.; Kroupa, N.; Kullgren, J.; Kuner, M. C.; Kuryla, D.; Liepuoniute, G.; Lin, C.; Margraf, J. T.; Magdău, I. B.; Michaelides, A.; Moore, J. H.; Naik, A. A.; Niblett, S. P.; Norwood, S. W.; O'Neill, N.; Ortner, C.; Persson, K. A.; Reuter, K.; Rosen, A. S.; Rosset, L. A. M.; Schaaf, L. L.; Schran, C.; Shi, B. X.; Sivonxay, E.; Stenczel, T. K.; Sutton, C.; Svahn, V.; Swinburne, T. D.; Tilly, J.; van derOord, C.; Vargas, S.; Varga-Umbrich, E.; Vegge, T.; Vondrák, M.; Wang, Y.; Witt, W. C.; Wolf, T.; Zills, F.; Csányi, G. A Foundation Model for Atomistic Materials Chemistry. *J. Chem. Phys.* **2025**, *163*, 184110.
(76) Zuo, Y.; Chen, C.; Li, X.; Deng, Z.; Chen, Y.; Behler, J.; Csányi, G.; Shapeev, A. V.; Thompson, A. P.; Wood, M. A.; Ong, S. P. Performance and Cost Assessment of Machine Learning Interatomic Potentials. *J. Phys. Chem. A* **2020**, *124* (4), 731–745.
(77) Erlebach, A.; Šípka, M.; Saha, I.; Nachtigall, P.; Heard, C. J.; Grajciar, L. A Reactive Neural Network Framework for Water-Loaded Acidic Zeolites. *Nat. Commun.* **2024**, *15* (1), 4215.
(78) Moodley, D.; Potgieter, J.; Moodley, P.; Crous, R.; van Helden, P.; van Zyl, L.; Cunningham, R.; Gauché, J.; Visagie, K.; Botha, T.; Claeys, M.; van Steen, E. Tuning the Active Sites of Supported Cobalt Fischer-Tropsch Catalysts to Enhance Efficiency for Hard Wax Production. *Catal. Today* **2025**, *454*, 115282.
(79) Tucker, C.; van Steen, E. Effect of Crystallite Size Distribution on the Oxidation and Re-Reduction of Cobalt in the Fischer–Tropsch Synthesis: A Thermodynamic Analysis. *Catal. Lett.* **2021**, *151* (9), 2631–2637.
(80) Blekkan, E. A.; Ivanez, O.; Van Valen, Y.; Gopakumar, J.; Herold, F.; Rønning, M. Characterization Study of Cobalt–manganese Catalysts for Fischer–Tropsch Synthesis, **2025**.
(81) Lide, D. R. Ionization Potentials of Atoms and Atomic Ions – Section 10. Atomic, Molecular, and Optical Physics. In *CRC Handbook of Chemistry and Physics*; **2003**, pp 10–180.
(82) Janse Van Rensburg, W.; Van Helden, P.; Moodley, D. J.; Claeys, M.; Petersen, M. A.; Van Steen, E. Role of Transient Co-Subcarbonyls in Ostwald Ripening Sintering of Cobalt Supported on γ-Alumina Surfaces. *J. Phys. Chem. C* **2017**, *121* (31), 16739–16753.
(83) Claeys, M.; Dry, M. E.; Van Steen, E.; Van Berge, P. J.; Booyens, S.; Crous, R.; Van Helden, P.; Labuschagne, J.; Moodley, D. J.; Saib, A. M. Impact of Process Conditions on the Sintering Behavior of an Alumina-Supported Cobalt Fischer-Tropsch Catalyst Studied with an in Situ Magnetometer. *ACS Catal.* **2015**, *5* (2), 841–852.
(84) Moodley, D.; Claeys, M.; van Steen, E.; van Helden, P.; Kistamurthy, D.; Weststrate, K. J.; Niemantsverdriet, H.; Saib, A.; Erasmus, W.; van de Loosdrecht, J. Sintering of Cobalt during FTS: Insights from Industrial and Model Systems. *Catal. Today* **2020**, *342*, 59–70.

(85) Kistamurthy, D.; Saib, A. M.; Moodley, D. J.; Niemantsverdriet, J. W.; Weststrate, C. J. Ostwald Ripening on a Planar Co/SiO_2 Catalyst Exposed to Model Fischer-Tropsch Synthesis Conditions. *J. Catal.* **2015**, *328*, 123–129.
(86) van Koppen, L. M.; Iulian Dugulan, A.; Leendert Bezemer, G.; Hensen, E. J. M. Sintering and Carbidization under Simulated High Conversion on a Cobalt-Based Fischer-Tropsch Catalyst; Manganese Oxide as a Structural Promotor. *J. Catal.* **2022**, *413*, 106–118.
(87) Zhang, Z.; Gee, W.; Lavroff, R. H.; Alexandrova, A. N. GOCIA a Grand Canonical Global Optimizer for Clusters, Interfaces, and Adsorbates. *Phys. Chem. Chem. Phys.* **2025**, *27* (2), 696–706.

https://doi.org/10.1021/acscatal.6c04886
ACS Catal. XXXX, XXX, XXX–XXX